Journal of South American Earth Sciences 104 (2020) 102858

Contents lists available at ScienceDirect

Journal of South American Earth Sciences

journal homepage: www.elsevier.com/locate/jsames

# Interpreting detrital modes and geochemistry of sandstones from the late Paleozoic Tepuel-Genoa Basin: Paleogeographic implications (Patagonia, Argentina)

Patricia L. Ciccioli [a,b,*], Carlos O. Limarino [a,b], John L. Isbell [c], Arturo C. Taboada [d], María A. Pagani [e], Erik L. Gulbranson [f]

[a] Universidad de Buenos Aires, Facultad de Ciencias Exactas y Naturales, Departamento de Ciencias Geológicas, Ciudad Universitaria, Pab. 2, 1° Piso, Buenos Aires, Argentina
[b] CONICET-Universidad de Buenos Aires, Instituto de Geociencias Básicas, Aplicadas y Ambientales de Buenos Aires (IGEBA), Buenos Aires, Argentina
[c] University of Wisconsin-Milwaukee. Milwaukee, Wisconsin, USA
[d] Centro de Investigaciones Esquel de Montaña y Estepa Patagónicas (CIEMEP)-CONICET. Roca 780, Esquel, Chubut, Argentina
[e] CONICET-Museo Paleontológico "Egidio Feruglio" (MEF), Av. Fontana No. 140, Trelew (U9100GYO), Chubut, Argentina
[f] Gustavus Adolphus College, St. Peter, Minnesota, USA

A B S T R A C T

The provenance of sandstones deposited in the late Paleozoic Tepuel-Genoa Basin is analyzed in this paper. Five sections were sampled in Esquel, Sierra de Tepuel, Sierra de Tecka, El Molle, and Río Genoa areas for petrographic and geochemical studies. The sandstones in the Tepuel-Genoa Basin are dominated by feldspathic litharenites and litharenites, showing lithic fragments of volcanic and sedimentary rocks in the Valle Chico Formation and medium-to high-grade metamorphic rock clasts in the rest of the units.

Detrital modes of seventy-five sandstones samples from the Valle Chico, Pampa de Tepuel, Mojón de Hierro, and Río Genoa formations were counted and analyzed. Seven modal components have discriminant value for identifying provenance areas (Qm, Qi, Lv, Lmm-h, Lm-Lp, Lm, Qpm). These modal components allow identification of three petrofacies: 1. Quartzose-lithic ($Qm_{69}Lv_2Lm_{29}$), 2. Quartzose ($Qm_{89}Lv_4Lm_7$) and 3. Volcanic-sedimentary ($Qm_{60}Lv_{38}Lm_1$). The quartzose-lithic petrofacies is mainly composed of monocrystalline quartz, medium- and high-grade metamorphic clasts and polycrystalline quartz with cataclastic texture, this assemblage is interpreted as being derived from the crystalline rocks that form the Deseado Massif. The quartzose petrofacies is composed of monocrystalline quartz with scarce contributions of metamorphic clasts and traces of volcanic fragments; the provenance area is ascribed to sedimentary terrains, which most likely covered part of the Deseado Massif. The volcanic-sedimentary petrofacies is comprised of volcanic (acidic and intermediate rocks) and sedimentary (sandstone and mudstone) clasts, with discrete amounts of quartz grains with idiomorph shapes and embayments. This assemblage may correspond to material supply from the Devonian-Early Carboniferous accretionary complex developed in Chile or the unroofing of the western volcanic arc located in the central part of Patagonia. The validity of the three defined petrofacies was evaluated using Principal Component Analysis and triangular compositional diagrams; both methods show good separation and lack of overlap between the three petrofacies. Major (Si, Al, Fe, Na, K) and trace-REE elements (Zr, Th, Sc, Hf) were used to improve the petrographic information. The relation $SiO_2$ against $K_2O/Na_2O$ indicates that the Pampa de Tepuel and the Mojón de Hierro formations correspond to a passive margin, while the Valle Chico and Río Genoa formations represent different types of active continental margins. The Th/Sc and Zr/Sc ratios and the Th-Hf-Co distributions indicate that the sandstones of the Tepuel Group were formed from rocks compatibles with the average composition of the upper continental crust.

## 1. Introduction

The Tepuel-Genoa Basin, located in the west of Argentinian Patagonia (Fig. 1), is a key depositional area for interpreting the evolution of the southwestern margin of Gondwana during the late Paleozoic. From the biostratigraphic point of view, this basin exposes one of the most complete records of late Paleozoic marine faunas in the Andean region (González, 1985, Simanauskas and Sabattini, 1997; Taboada et al., 2018, 2019), and contains one of the richest Early Permian megafloras in southern South America (Andreis and Cúneo, 1989; Escapa and Cúneo, 2003). Moreover, the transition from Late Devonian to earliest Carboniferous (Tournaisian), which is poorly exposed in the southwestern margin of Gondwana, seems to be present in the Esquel and Valle Chico formations (Taboada et al., 2019). The Tepuel-Genoa Basin

* Corresponding author. CONICET-Universidad de Buenos Aires, Instituto de Geociencias Básicas, Aplicadas y Ambientales de Buenos Aires (IGEBA), Buenos Aires, Argentina.
*E-mail address:* ciccioli@gl.fcen.uba.ar (P.L. Ciccioli).

https://doi.org/10.1016/j.jsames.2020.102858
Received 2 June 2020; Received in revised form 28 August 2020; Accepted 29 August 2020
Available online 3 September 2020

also exposes diamictites containing faceted-striated clasts and shales bearing dropstones formed during the glacial event that affected Gondwana during the late Paleozoic (López Gamundí, 1989, López Gamundí et al., 1992; Isbell et al., 2003, 2012).

Beyond the above-mentioned items, several issues concerning the paleogeography, tectonic setting, and magmatic evolution of the Tepuel-Genoa Basin remain under debate. For example, the existence of Patagonia as an exotic microcontinent has been largely debated. While Winter (1984) and Ramos (1984, 2008) and Ramos et al. (1986) considered Patagonia as an accreted terrane during the Paleozoic, other authors interpreted the eastern part of the North Patagonian Massif as a parautochthonous terrain (Rapalini et al., 2010; González et al., 2018), while Forsythe (1982) and Dalla Salda et al. (1990) considered Patagonia as an autochthonous block.

Moreover, the Tepuel-Genoa Basin has been subjected to different interpretations; it was considered as a foreland basin that developed on the passive margin of the Deseado Massif during the collision with the North Patagonian Massif (Pankhurst et al., 2006). On the contrary, Ramos (2008) described the Tepuel-Genoa Basin as a forearc basin that developed between a Devonian-Carboniferous accretionary prism and a western magmatic arc (Ramos et al., 1986: Fig. 12a). Renda et al. (2019) presented an alternative interpretation, in which the Deseado Massif and the Tepuel-Genoa Basin were part of an allochthonous block located away from South America, near the southwest margin of Antarctica, during the late Paleozoic.

The study of sediment provenance helps to decipher the tectonic and paleogeographic evolution of Patagonia during the late Paleozoic. Some papers have been published in the last years using U–Pb detrital zircon ages for interpreting the provenance areas of late Paleozoic rocks (Duhart et al., 2002; Hervé et al., 2003; Pankhurst et al., 2006; Griffis et al., 2019) and some abstracts about sedimentary petrology (Ciccioli et al., 2018a,b). Nevertheless, an integral analysis of the detrital modes of late Paleozoic sandstones has not been performed yet, which does not allow obtaining a complete lithological characterization of sediment supply areas, thus hampering paleogeographic reconstructions.

In this paper, we presented the first study of the detrital modes of sandstones and the geochemical features of the Tepuel-Genoa Basin. This type of study allows a better interpretation and understanding of the complex source areas that supplied sediment to the basin.

## 2. Regional setting

The Tepuel-Genoa Basin is located in the western part of Argentinian Patagonia in the southernmost part of South America (Fig. 1). For understanding the history of the Tepuel-Genoa Basin, it is necessary to consider the regional context, in particular, the nature of pre-Carboniferous basement rocks, the presence of a belt of Carboniferous and Permian granitoids, and the existence of a thick, highly deformed accretionary prism along the western margin of the basin in Chile (Pankhurst et al., 2006; Hervé et al., 2013, 2016; Ramos and Naipauer, 2014).

These features are displayed in the sketch map of Patagonia in Fig. 2, which shows the two main basement blocks corresponding to the North Patagonian and Deseado massifs. The northern boundary of Patagonia is marked by a lineament that delineates a sharp change in the thickness of the crust, to the north a thicker Gondwana crust (Río de La Plata Craton), and to the south a thinner and younger crust corresponding to Patagonia (Fig. 1; Ramos, 1996, 2008; Kostadinoff et al., 2005).

The basement of the North Patagonian Massif, called "Nesocratón Nordpatagónico" by Harrington (1962), is composed of Precambrian metamorphic rocks and granitoids, Ordovician granites, Cambro-Ordovician low-grade metamorphic rocks and meta-sediments of Silurian and Devonian ages (metagraywackes, slates, Fig. 2).

A second basement block corresponds to the Deseado Massif, which is mainly made up of a suite of igneous-metamorphic rocks that consist of slates, schists, gneisses, and granitoids (Complejo Río Deseado, Viera and Pezzuchi, 1976; Giacosa et al., 2002). These rocks are covered by late Paleozoic sandstones and conglomerates of the La Golondrina Formation.

The western part of Patagonia was almost entirely developed in Chile and corresponds to accretionary complexes resulting from Devonian to the early Mesozoic polydeformational and polymetamorphic events

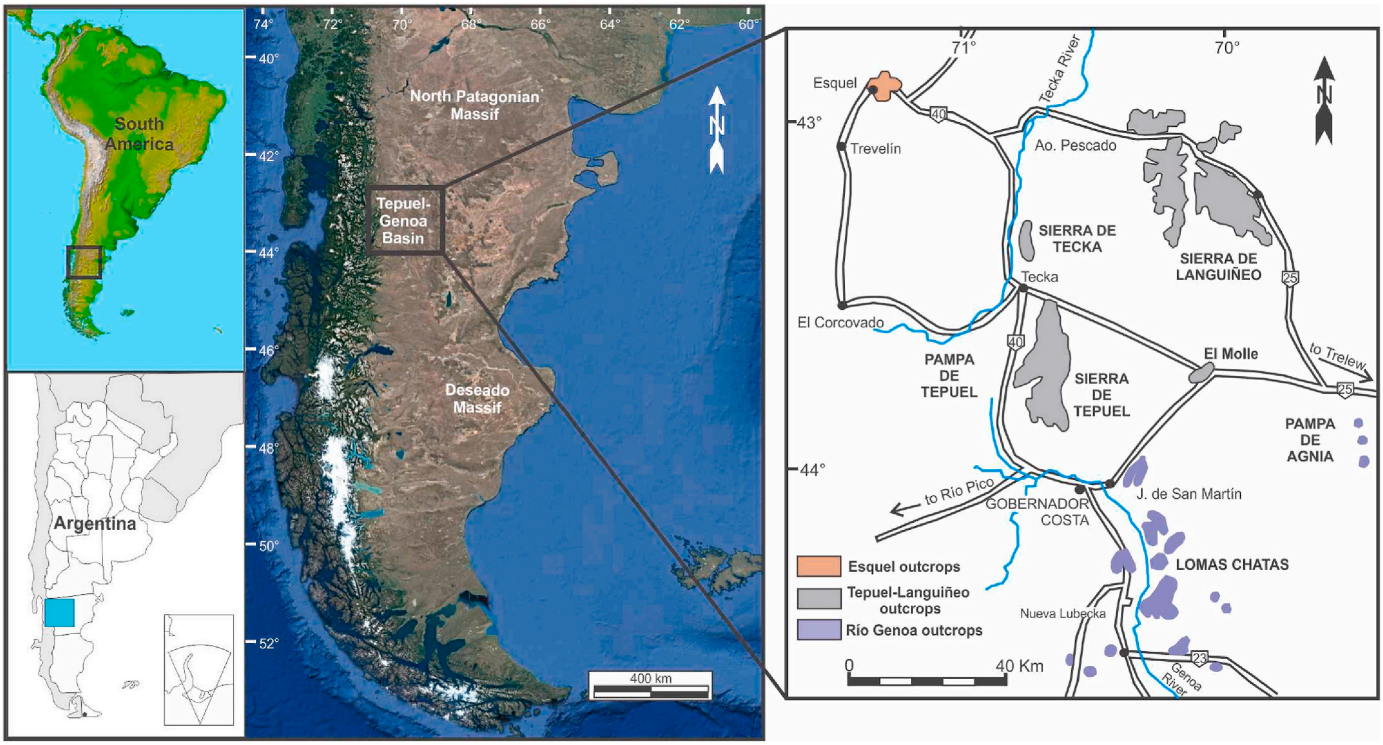


**Fig. 1.** Location of the Tepuel-Genoa Basin in Patagonia, to the right distribution of the main outcrops of the Tepuel Group.

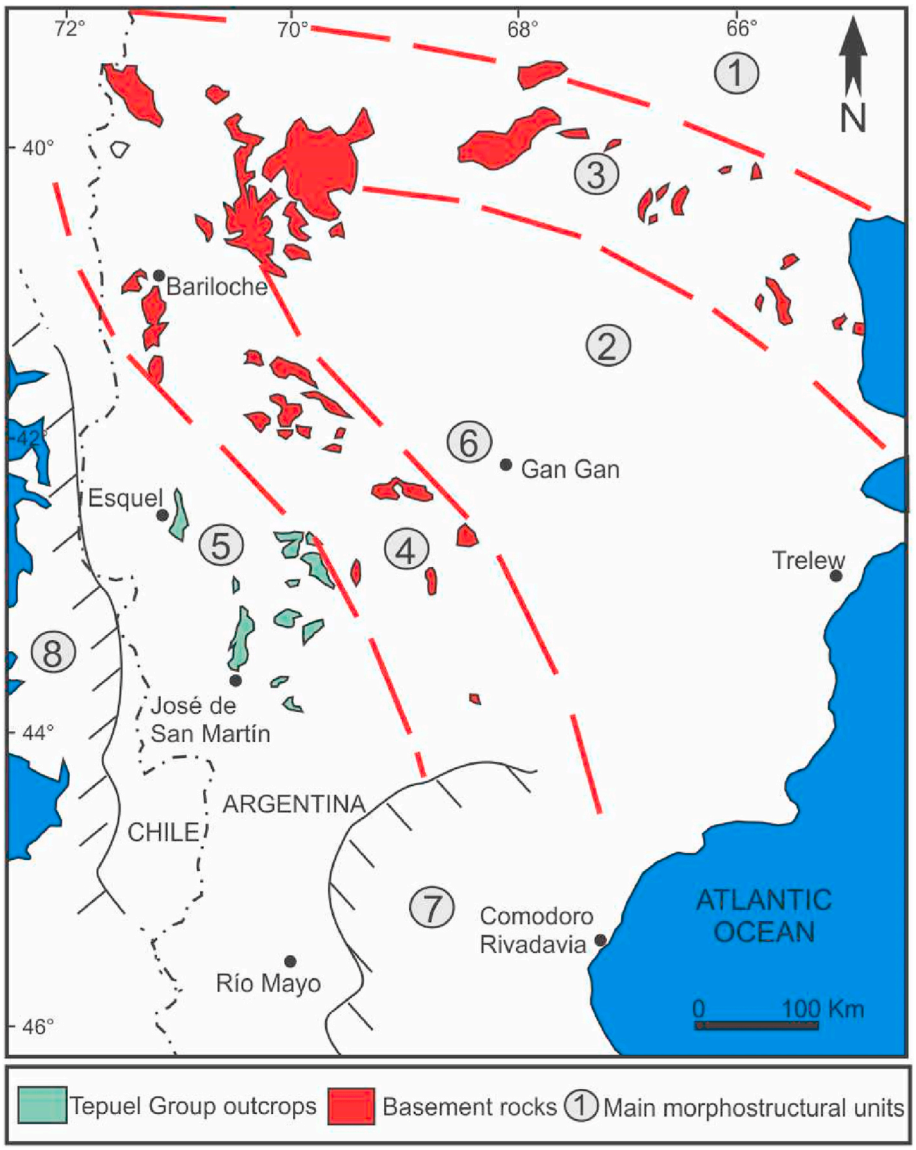


**Fig. 2.** Main morphostructural features of Patagonia showing the relative position of the Tepuel Group. References: 1: Río de la Plata Craton, 2: North Patagonian Massif, 3. Northern magmatic arc, 4. Western magmatic arc, 5. Tepuel-Genoa Basin, 6. Deformed Paleozoic belt (including mylonites), 7. Deseado Massif, 8. Paleozoic accretionary complex in Chile.

(Hervé et al., 2013, 2016, Fig. 2). This accretionary complex is composed of highly deformed schists, meta-basites, meta-cherts, and metasedimentary rocks (including some meta-sandstones, meta--diamictites, and slates). An interesting aspect is the existence of granitic and volcanic rocks attributed to magmatic arcs that formed in double (Devonian) and single (early Carboniferous) subduction zones (Hervé et al., 2016).

Pankhurst et al. (2006) and Ramos (2008), among others, considered the origin, significance, and extension of a northwest-southeast belt of Devonian and Carboniferous granites in Patagonia (Fig. 2). Pankhurst et al. (2006) described these intrusive bodies as I-type and S-type granites formed during the collision of the Deseado Massif against the North Patagonian Massif. An alternative possibility was proposed by Ramos (2008), who interpreted these granites as part of a Devonian-mid Carboniferous volcanic arc ("Western magmatic arc" by Ramos, 2008, Fig. 2), linked to the collision of the Antarctic Peninsula with Patagonia.

Regionally an interesting suite of metamorphic rocks associated with the granitoids occurs, in which at least four metamorphic events were dated (Cerredo and López de Luchi, 1998, Fig. 2). Part of these metamorphic rocks corresponds to the Cushamen Formation composed of meta-sandstones, meta-diamictites, meta-volcanics, and meta-schists (for synthesis, see Marcos et al., 2018). Although the age of the Cushamen Formation is still under debate, at least part of this unit may be Carboniferous, according to a Visean age obtained by Hervé et al. (2005). Considering this maximum depositional age, Marcos et al. (2018) correlated the Cushamen Formation with the glaciogenic section of the Tepuel Group.

## 3. The Tepuel-Genoa Basin

The Tepuel-Genoa Basin (about 10.000 km$^2$ large) is a late Paleozoic basin that extends from the foot of the Patagonian Andes in the west (Esquel outcrops), to the extra-Andean Patagonia in the east (Pampa de Agnia-El Molle sections, Fig. 1). Here, the basin is divided into three areas; the northwestern outcrops correspond to the 600 m thick Valle Chico Formation (Cucchi and Askenasy, 1982, Fig. 3), which is composed of diamictites, shales with dropstones, mudstones, fine- and medium-grained sandstones together with scarce conglomerates and coarse-grained sandstones (Figs. 3 and 4b). This unit was deposited in marine environments; it mainly corresponds to monotonous successions

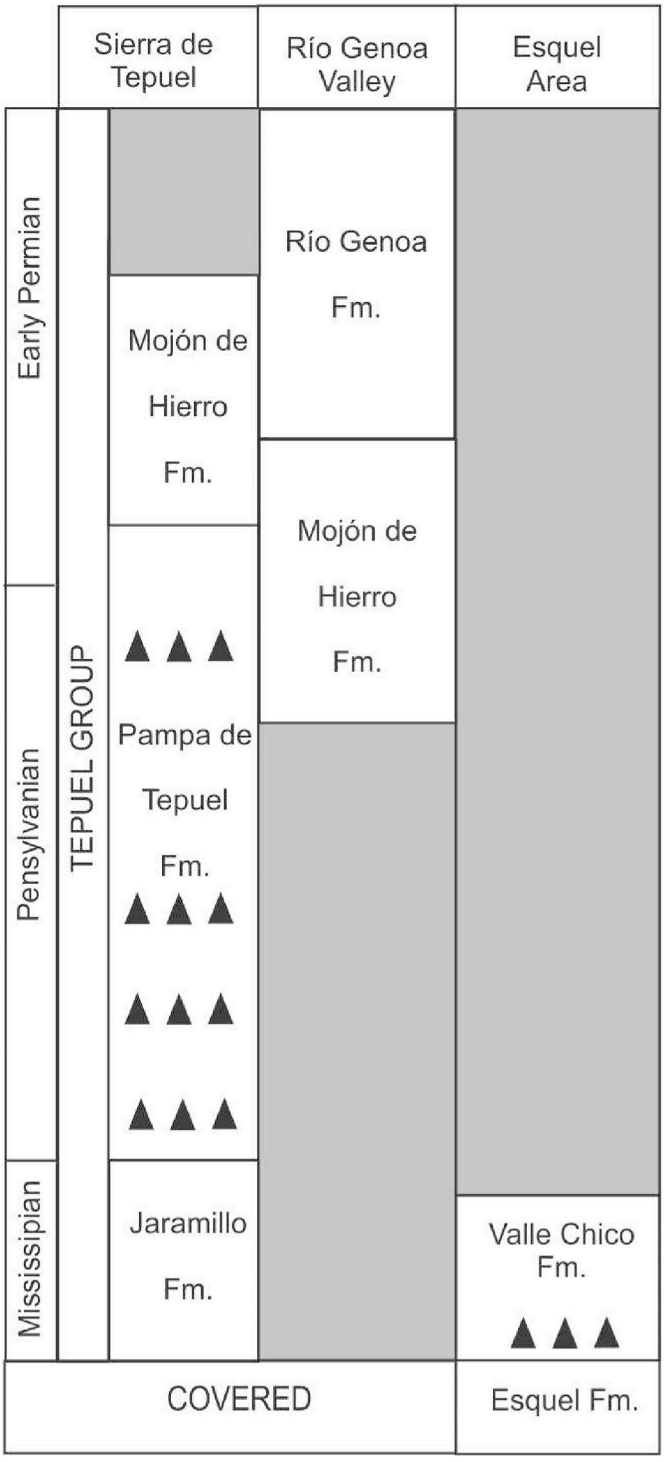


**Fig. 3.** Stratigraphy of the Tepuel Group, black triangles indicate the position of glacigenic-related diamictites.

of offshore shales with thin sandy intercalations formed during storm events (López Gamundí, 1980; González Bonorino and González Bonorino, 1988). Towards the middle and upper part, thin intercalations of fluvio-deltaic sandstones and mudstones containing plant remains and invertebrate fossils are found. Although subglacial or ice contact deposits have not been identified, the influence of glacial conditions is pointed out not only by the presence of dropstones but also by the frequent occurrence of faceted and striated clasts in the diamictites (López Gamundí, 1980; González Bonorino and González Bonorino, 1988).

The central part of the basin comprises outcrops distributed along the Sierra de Languiñeo, Sierra Tecka, and Sierra de Tepuel (Figs. 1 and 3). The stratigraphy of the late Paleozoic in this area was described by Suero (1953), Chebli et al. (1979), and Page et al. (1984), among others. These authors included the whole Carboniferous-Permian sequence in the Tepuel Group, which was divided into the Jaramillo (Mississippian), the Pampa de Tepuel (Late Mississippian-Pennsylvanian) and the Mojón de Hierro (Late Pennsylvanian-early Permian) formations. Recently, Taboada et al. (2019) proposed that the Pampa de Tepuel Formation reaches the early Permian in the Sierra de Tepuel (Fig. 3).

The Jaramillo Formation only crops out in the Sierra de Tepuel and is composed of sandstones, mudstones, and some levels of diamictites. The origin of the unit was scarcely studied, but the presence of mudstones and shales with remains of *Archaeosigillaria conferta* flora suggests a continental (fluvio-deltaic) depositional environment at least for part of the succession (Fig. 3).

The Pampa de Tepuel Formation crops out throughout the region and is composed of shales, shales with dropstones, fine- and medium-grained sandstones (rarely coarse-grained), and several levels of diamictites bearing faceted and striated clasts up to 30 cm in diameter (Fig. 4b). The Pampa de Tepuel Formation is interpreted as deposited in glacially influenced marine shelf, slope and basin floor environments, in which mass transport deposits and outwash submarine fans were formed (López Gamundí and Limarino, 1984; González Bonorino, 1992; Limarino et al., 1999, 2020a; Pauls, 2014; Survis, 2015).

The top of the Tepuel Group in the Sierra de Tepuel and Sierra de Languiñeo corresponds to the Mojón de Hierro Formation that mainly comprises fine- and medium-grained sandstones together with shales, marls, and some levels of limestones (Figs. 3 and 4c). This unit probably corresponds to a large-scale progradational cycle, that begins with deep water deposits and ends with shallow marine deposits, and deltaic successions at the top (Andreis and Cúneo, 1985; MacNall, 2019; Limarino et al., 2020a).

Late Paleozoic strata of the Río Genoa Formation occurs in the southern part of the Tepuel-Genoa Basin (Río Genoa and Lomas Chatas areas, Figs. 1 and 3). This unit is composed of conglomerates, coarse-to fine-grained sandstones, mudstones, and carbonaceous mudstones (Fig. 4d and e). The Río Genoa Formation was deposited in a highly constructive delta, with short marine transgressions that bounded progradational and aggradational sequences (Cortiñas and Arbe, 1982). According to Andreis et al. (1985), the Río Genoa Formation correlates with the middle and upper parts of the Mojón de Hierro Formation in the Sierra de Tepuel (Fig. 3).

## 4. Methodology

Five sections were sampled in the Esquel, Sierra de Tepuel, Sierra de Tecka, El Molle, and Río Genoa areas, to obtain regional information about the composition of the sandstones along the Tepuel-Genoa Basin (Fig. 1). Seventy-five unaltered medium- and coarse-grained sandstones come from the Valle Chico, Pampa de Tepuel, Mojón de Hierro, and Río Genoa formations. All the samples were analyzed for diagenetic features, including authigenic minerals, dissolution processes, and porosity patterns. To avoid diagenetic modifications in the original detrital modes, three sandstones samples showing a high amount of matrix (more than 10%) and pervasive replacement of clasts were discarded. All the sandstones were impregnated in blue epoxy resin before slabbing and grinding to aid in identifying porosity. The percentages of optical porosity were measured using the petrographic image analysis JMicrovision1.27 program. Besides, thin sections were stained with alizarin red and potassium ferricyanide for differentiation of carbonate cement.

Modal components used during point count, and recalculated parameters, are shown in Tables 1–3. Highly altered grains, or grains pervasively replaced by authigenic minerals were counted as undetermined grains, while quartz or feldspar overgrowths were recorded as

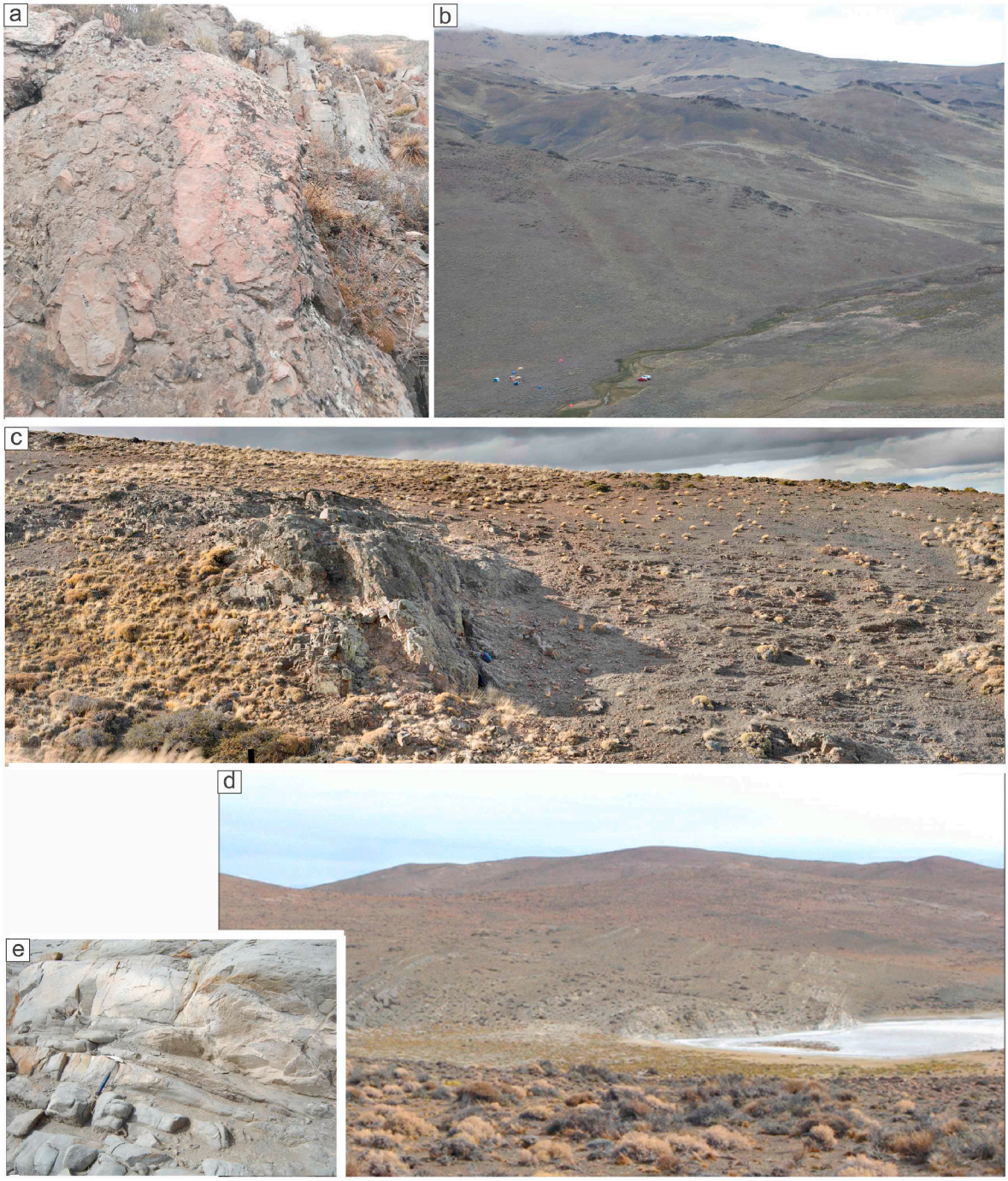


**Fig. 4.** View of the different units that form the Tepuel Group, a. basal diamictite of the Valle Chico Formation bearing large clasts of granitic and volcanic rocks, b. outcrops of the Pampa de Tepuel Formation in the Sierra de Tepuel, note the abundance of deep water shales and some sandstones that make up the ridges (hard beds), c. an aspect of the lower Mojón de Hierro Formation at Arroyo Garrido showing sandstones, diamictites, and shales to the right, d. view of the Río Genoa Formation developing low-relief hills in the Salar de Ferrarotti, e. details of the interbedded sandstones and mudstones in the Río Genoa Formation (hammer as scale).

cement. Quartz (Q) grains were separated into monocrystalline (Qm) and polycrystalline (Qp) types (Table 1). At the same time, monocrystalline quartz was divided into monocrystalline quartz (Qm, Fig. 5a) and idiomorph monocrystalline quartz (Qmi) due to the presence of idiomorph shapes and negative crystals (Table 1). Polycrystalline quartz (Qp) comprises three categories: coarse-grained (Qpg, Fig. 5b), mylonitic (Qpm, Fig. 5c), and fine-grained (Qpf, Table 1). Among the feldspars (F), K-feldspar (orthoclase, O, Fig. 5d), microcline (M, Fig. 5f), and plagioclase (P, Fig. 5e) were recognized (Table 1). Feldspars with perthites or with mineral intergrowths were observed but not separately counted. Rock fragments (L) include volcanic (Lv), metamorphic (Lm), and sedimentary (Ls) lithics. In turn, volcanic grains were divided according to their textures reflecting different magma compositions (e.g., Dickinson, 1970; Critelli and Ingersoll, 1995). Thus, we recognized volcanic lithics with felsitic (Lva), microlitic (Lvm, Fig. 5g), lathwork (Lvb, Fig. 5h) textures as well as altered volcanics (Lvalt, Table 1).

Metamorphic fragments (Lm) were separated into low-grade (Lml, Fig. 6a), including phyllites and slates, and medium-to high-grade (Lmm-h, Fig. 6b and c) that include schists and amphibolites. Sedimentary rock fragments (Ls) were categorized as sandstones (Lss,

**Table 1**
Modal components and recalculated parameters for the sandstones of the Tepuel Group.

| Modal component | Explanation: Clast composition | Recalculated parameters |
|---|---|---|
| Qm | Monocrystalline quartz (single crystals) | |
| Qmi | Idiomorph monocrystalline quartz (single crystals) | Qmt (total monocrystalline quartz) = Qm + Qmi |
| QPg | Polycrystalline coarso-grainod quartz | Qpt (total polycrystallyno quartz)- Qpg + Qpf + Qpm |
| Qpf | Polycrystalline fine-grained quartz | Q (total quartz) = Qmt + Qpt |
| Qpm | Polycrystalline cataclastic quartz (milonites) | |
| O | K-Feldespar orthoclase and sanidine | F (total feldspar) = O + M + P |
| M | K-Feldspar microcline | |
| P | Plagioclase | LVT (total volcanic clast) - Lva f Lvm + Lvb + Lvalt |
| Lva | Volcanic clast with felsitic texture | LMT (total metamorphic ctasts) = Lml + Lmm-h + Lp-Lm |
| Lvm | Volcanic clast with mlcrolitlc texture | LST (total sedimentary clasts) - Lss + Lsw + Lsf |
| Lvb | Volcanic clast with lathwork texture | |
| Lvalt | Altered volcanic clast | Signal of the crystalline basament supply = Lmm-h + (Lm-Lp) + Qpm |
| Lml | Low-grade metamorphic | |
| Lmm-h | Medium- and high-grade metamorphic | Signal of the volcanic-sedimentary supply = Lv + Lsw + Qi |
| Lp-Lm | Gneisses and granitoids | |
| Lss | Matrix-free sandstone | Signal of the sedimentary terrains supply = Qm + Lss |
| Lsw | Wacke | |
| Lsf | Mudstone | |

Fig. 6e), wackes (Lsw, Fig. 6f), and mudstones (Lsf). Finally, plutonic-metamorphic fragments (Lp-Lm, Fig. 6d) were separately identified (Table 1). Accessory minerals, including micas (biotite and muscovite), amphiboles, pyroxenes, zircons, and opaques, were counted but not used for provenance studies.

A minimum of 350 points were counted for each thin section, separating monocrystalline and polycrystalline framework clasts. In this last case (monocrystalline vs polycrystalline), we used the Gazzi-Dickinson methodology to avoid compositional variations resulting from different grain sizes (in Zuffa, 1985; Weltje, 2002).

Geochemical analysis for major, minor, and trace elements was obtained in fifteen fresh samples that showed a low percentage of cement and matrix in the sample selected after an initial petrographic analysis. These samples correspond mainly to medium-to coarse-grained sandstones. All samples were analyzed by ActLabs in Canada using a combination of FUS-ICP and FUS-MS methods. The geochemistry of the sandstones was used not only as a complementary way to identify source areas but was also used to establish comparations between the petrographic and geochemical methods.

## 5. Sandstone petrology

### 5.1. Sandstone composition

From the petrographic point of view, the studied sandstones must be divided into two groups. Firstly, those sandstones belonging to the Valle Chico Formation (Esquel area), which correspond to litharenites and less frequently feldspathic litharenites, and lithic feldsarenites (Qm33:Ft13:Lt50, Folk et al., 1970, Tables 2 and 3, Fig. 7a and b). These sandstones are dominated by lithic fragments (33% on average) composed of sedimentary (mudstones rarely very fine-grained sandstones) and volcanic clasts, with subordinate proportions of metamorphic grains. The amount of quartz grains is moderate, mainly monocrystalline (33%) and scarce polycrystalline (2%); in some cases, monocrystalline quartz displays idiomorph shapes and negative crystals that suggest volcanic derivation. The total amount of feldspar is 13%, with the K-feldspar (orthoclase) percentages occurring higher than the plagioclase (oligoclase-andesine) in almost all the samples.

In the central area of the Tepuel-Genoa Basin (Pampa de Tepuel and Mojón de Hierro formations), sandstones increase in the amount of both monocrystalline (46%) and polycrystalline quartz (4%) compared to sandstones in the Valle Chico Formation (Fig. 7a and b). At the same time, idiomorph quartz clasts bearing negative crystals are very scarce, and the proportion of volcanic fragments is minor. Sandstones of the Pampa de Tepuel Formation correspond to feldspathic litharenites and litharenites with few lithic feldsarenites (Qm44:F18:Lt38 on average) while the Mojón de Hierro Formation sandstones correspond mainly to litharenites and feldspathic litharenites with scarce sublitharenites and lithic feldsarenites (Qm52:F11:Lt37 on average) (Table 3 and Fig. 7a). An increase of total quartz grains (Q) in the Mojón de Hierro Formation (61%) with respect to the Pampa de Tepuel Formation (44%) was observed. Feldspars are dominated by orthoclase, together with scarce microcline, (ratio plagioclase/K-feldspar is generally less than 1, Table 3). The amount of lithic fragments in these sandstones is significant (about 37% on average), corresponding to low-grade metamorphic rocks (mainly slates) and sedimentary fragments (mudstones). The distinction between these two types of clasts is frequently problematic so that both types of fragments should be included in the same category.

The southern part of the Tepuel-Genoa Basin corresponds to the Río Genoa Formation, as in the central area of the basin to the Pampa de Tepuel and the Mojón de Hierro formations. The sandstone composition for the Río Genoa Formation is dominated by feldspathic litharenites and lithic feldsarenites (Qm35:Ft24:Lt41 on average) with scarce litharenites and only one feldsarenite (Fig. 7a and b and Table 3). The Río Genoa Formation exhibits the higher amounts of both K-feldspar and plagioclase (24% in total) and a little decrease in the percentage of quartz clasts (35%) when compared with the central part of the basin (the Pampa de Tepuel and Mojón de Hierro formations). The monocrystalline quartz content is similar to that observed in the Valle Chico Formation, but idiomorph quartz clasts are very scarce in the Río Genoa Formation.

Another characteristic of the Río Genoa Formation is the presence of significant proportions of metamorphic clasts, including grains derived from slates, micaceous and quartz-feldspathic schists as well as medium- to high-grade metamorphic clasts (Table 2; Fig. 7b).

### 5.2. Diagenetic features

The main diagenetic features of the sandstones were identified to evaluate the impact of the diagenesis on the original detrital modes. Three subjects will be considered: 1. The relation of authigenic minerals (mainly cement) with the framework clasts, 2. The effect of the compaction over ductile grains and 3. The origin of the secondary porosity.

In the central and southern parts of the basin (Pampa de Tepuel, Mojón de Hierro, and Río Genoa formations), two types of cement assemblages occur: 1) siliceous cement (quartz overgrowths, megaquartz, and rarely microquartz) that widely dominate in quartz-rich sandstones (Fig. 8a and b), and 2) rim cement of chlorite-illite (Fig. 8c) and occluding cement of kaolinite in the lithic feldsarenites and feldsarenite. In sandstones of the Río de Genoa Formation traces of feldspar overgrowths were also observed (Fig. 8f and g).

In some sandstones, calcite occurs either as pore-filling intergranular cement or calcite patches as a replacement of clasts (Fig. 8d). Although this last type of calcite could mask the original composition of some clasts, the low amount of replacements and the fact that in many cases the replacement is only partial allows determining the original composition of the clasts.

In the case of the Valle Chico Formation, quartz overgrowths and

**Table 2**
Modal point-count data of the Tepuel Group sandstones.

| Samples | Qm | Qmi | Qpg | Qpm | Qpf | O | M | P | Lva | Lvm | Lvb | Lvalt | Lml | Lmm-h | Lss | Lsw | Lsf | Lp-Lm | Ac |
|---|---|---|---|---|---|---|---|---|---|---|---|---|---|---|---|---|---|---|---|
| Río Genoa Formation (n = 19) | | | | | | | | | | | | | | | | | | | |
| M130 | 15.35 | 0 | 3.94 | 15.75 | 0 | 4.33 | 0 | 0 | 0.79 | 0 | 0 | 0 | 24.8 | 33.07 | 0 | 0 | 0 | 1.97 | 0 |
| M132 | 41.78 | 0 | 8.9 | 0.68 | 0 | 5.48 | 0 | 3.42 | 0 | 0 | 0 | 0 | 20.59 | 18.15 | 0 | 0 | 0 | 0 | 1 |
| M132B | 38.78 | 0 | 12.24 | 0 | 0 | 7.48 | 1.36 | 0.68 | 0 | 0 | 0 | 0 | 22.45 | 13.61 | 0 | 0 | 0 | 2.04 | 1.36 |
| M134 | 44.44 | 0 | 14.58 | 2.78 | 0 | 12.5 | 0 | 5.56 | 0 | 0 | 0 | 0 | 12.5 | 7.64 | 0 | 0 | 0 | 0 | 0 |
| M136 | 31.51 | 0 | 6.85 | 0 | 0 | 28.08 | 0 | 10.96 | 0 | 0 | 0 | 0 | 6.85 | 14.38 | 0 | 0 | 0 | 0 | 1.37 |
| M137 | 41.94 | 0 | 3.23 | 0 | 0 | 17.42 | 1.29 | 10.97 | 0 | 0 | 0 | 0 | 12.26 | 10.97 | 0 | 0 | 0 | 0 | 1.94 |
| M139 | 37.26 | 0 | 4.25 | 0.94 | 0 | 11.32 | 0 | 20.75 | 0 | 0 | 0 | 0 | 16.98 | 6.13 | 0 | 0 | 2.36 | 0 | 0 |
| M141 | 29.89 | 0 | 4.6 | 0 | 0 | 27.01 | 5.75 | 16.09 | 0 | 0 | 0 | 0 | 2.3 | 12.07 | 0 | 0 | 0 | 0 | 2.3 |
| M143 | 33.01 | 0 | 2.87 | 0 | 0 | 30.62 | 0.48 | 4.78 | 0.48 | 0 | 0 | 0 | 21.05 | 6.22 | 0 | 0 | 0 | 0 | 0.48 |
| M145 | 28.37 | 0 | 3.85 | 3.37 | 0 | 4.81 | 1.92 | 5.77 | 0.48 | 0.48 | 0 | 0 | 38.94 | 11.06 | 0.48 | 0 | 0.48 | 0 | 0 |
| M147 | 30.58 | 0 | 15.53 | 0 | 0 | 11.65 | 0 | 2.91 | 0 | 0 | 0 | 0 | 26.21 | 6.8 | 1.94 | 0 | 2.43 | 1.94 | 0 |
| M148 | 27.4 | 0 | 4.11 | 0.46 | 0 | 14.16 | 0 | 4.57 | 0.8 | 0 | 0 | 0 | 30.14 | 17.81 | 0 | 0 | 0 | 0 | 0.5 |
| M149 | 36.49 | 0 | 5.21 | 2.37 | 0 | 9.95 | 0 | 3.32 | 0.47 | 0 | 0 | 0 | 29.86 | 11.85 | 0 | 0 | 0 | 0 | 0.47 |
| M151 | 29.45 | 0 | 4.11 | 0 | 0 | 21.92 | 6.16 | 19.86 | 0 | 0 | 0 | 0 | 5.48 | 10.27 | 1.37 | 0 | 0 | 0 | 1.37 |
| M152 | 64.23 | 0 | 8.99 | 1.535 | 0 | 6.37 | 0 | 1.1 | 0.44 | 0 | 0 | 0 | 1.42 | 0.44 | 0.22 | 0 | 2.41 | 0 | 0 |
| M153 | 36.55 | 0 | 4.06 | 3.05 | 0 | 11.68 | 0 | 11.17 | 0 | 0 | 0 | 0 | 16.75 | 10.15 | 0.51 | 0 | 0 | 5.08 | 1 |
| M155 | 26.57 | 0 | 1.93 | 1.45 | 0 | 14.01 | 0 | 11.11 | 0 | 0 | 0 | 0 | 18.36 | 24.15 | 0 | 0 | 0.48 | 1.93 | 0 |
| M157 | 28.22 | 0 | 5.45 | 0 | 0 | 14.36 | 5.45 | 8.42 | 0 | 0 | 0 | 0 | 30.69 | 3.96 | 0 | 0 | 0 | 3.47 | 0 |
| M163 | 30.13 | 0 | 6.28 | 0 | 0 | 21.34 | 0 | 16.74 | 2.09 | 0 | 0 | 0 | 16.74 | 4.6 | 0 | 0 | 0 | 2.09 | 0 |
| Average | 34.3 | 0,0 | 6,4 | 1,7 | 0,0 | 14,4 | 1.17 | 8.32 | 0.29 | 0.02 | 0,0 | 0,0 | 19,3 | 11,8 | 0,2 | 0,0 | 0,4 | 1,0 | 0,6 |
| Std dv | 9.6 | 0,0 | 3,8 | 3,5 | 0,0 | 7,8 | 2.07 | 6.27 | 0.5 | 0.1 | 0,0 | 0,0 | 9,2 | 7,4 | 0,5 | 0,0 | 0,9 | 1,4 | 0,7 |
| Mojón de Hierro Formation (n = 18) | | | | | | | | | | | | | | | | | | | |
| M61 | 69.59 | 0 | 3.09 | 6.7 | 0.52 | 4.12 | 0 | 1.03 | 4.64 | 0 | 0 | 0 | 9.79 | 0 | 0 | | 0 | 0 | 0.51 |
| M62 | 66 | 0 | 2 | 10 | 1.5 | 1.5 | 0 | 4 | 0 | 0 | 0 | 6.5 | 0.5 | 7 | 0 | | 1 | 0 | 0 |
| M63 | 44.91 | 0 | 9.72 | 18.52 | 0 | 0.93 | 0 | 1.85 | 0 | 0 | 0 | 0 | 20.83 | 2.78 | 0 | | 0 | 0.46 | 0 |
| M66 | 52.63 | 0 | 6.77 | 0 | 0 | 3.76 | 0 | 6.02 | 2.26 | 0 | 0 | 0 | 18.8 | 7.52 | 0 | 0 | 2.26 | 0 | 0 |
| M68 | 46.26 | 0 | 6.8 | 0 | 0 | 6.12 | 0 | 8.84 | 0 | 0 | 0 | 0 | 15.65 | 16.33 | 0 | 0 | 0 | 0 | 0 |
| M89 | 27.86 | 0 | 1.99 | 0 | 0 | 3.98 | 0 | 4.48 | 0 | 0 | 0 | 0 | 50.75 | 10.95 | 0 | | 0 | 0 | 0 |
| M90 | 33.33 | 2 | 4.35 | 0 | 0 | 6.52 | 0.72 | 10.87 | 19.74 | 0 | 0 | 0 | 7.25 | 15.22 | 0 | 0 | 0 | 0 | 0 |
| M93 | 46.3 | 0 | 10.19 | 6.94 | 0 | 10.65 | 0 | 4.17 | 0 | 0 | 0 | 0 | 12.04 | 9.72 | 0 | | 0 | 0 | 0 |
| M94 | 44.44 | 0 | 4.04 | 6.06 | 0 | 4.55 | 0 | 3.54 | 0 | 0 | 0 | 0 | 11.11 | 26.26 | 0 | | 0 | 0 | 0 |
| M95 | 47.3 | 0 | 4.83 | 0 | 0 | 18.36 | 0.48 | 4.35 | 0 | 0 | 0 | 1.93 | 18.84 | 2.9 | 0 | | 0 | 0.97 | 0 |
| M99 | 60.71 | 0 | 2.86 | 3.57 | 0 | 2.14 | 1.43 | 5.71 | 0 | 0 | 0 | 0 | 20 | 3.57 | 0 | 0 | 0 | 0 | 0 |
| M104 | 72.09 | 0 | 1.55 | 11.63 | 0 | 3.88 | 0 | 1.55 | 0 | 0 | 0 | 0 | 9.3 | 0 | 0 | 0 | 0 | 0 | 0 |
| M108 | 61.48 | 0 | 5.19 | 0 | 6.67 | 0 | 4.44 | 1.48 | 0 | 0 | 0 | 0 | 8.15 | 10.37 | 0 | 0 | 2.22 | 0 | 0 |
| M111 | 58.79 | 0 | 2.51 | 2.01 | 0 | 17.09 | 0 | 3.02 | 2.51 | 1.01 | 0 | 0.5 | 8.54 | 0.5 | 3.02 | | 0 | 0.5 | 0 |
| M112 | 46.07 | 0 | 1.57 | 2.62 | 0 | 17.28 | 0 | 7.33 | 0 | 0 | 0 | 0.52 | 13.09 | 6.28 | 0 | | 0 | 0 | 5.24 |
| M122 | 60.75 | 0 | 7.01 | 1.4 | | 12.62 | 0 | 1.4 | 0 | 0 | 0 | 0 | 16.36 | 0.47 | 0 | | 0 | 0 | 0 |
| M126 | 31.82 | 0 | 0 | 0 | 0 | 4.55 | 0 | 2.27 | 0 | 0 | 0 | 0 | 22.73 | 38.64 | 0 | 0 | 0 | 0 | 0 |
| M129 | 61.54 | 0 | 6.15 | 0 | 0 | 2.31 | 0 | 0.77 | 0.77 | 0 | 0 | 0 | 20 | 8.46 | 0 | 0 | 0 | 0 | 0 |
| Average | 51.77 | 0.11 | 4.48 | 3.86 | 0.51 | 6.69 | 0.39 | 4.04 | 1.66 | 0.06 | 0,0 | 0.525 | 15.76 | 9.28 | 0.17 | 0,00 | 0.3 | 0.11 | 0.32 |
| Std dv | 12.6 | 0.46 | 2.78 | 5.09 | 1.58 | 5.74 | 1.05 | 2.75 | 4.55 | 0.23 | 0,0 | 1.52 | 10.24 | 9.72 | 0.69 | 0,00 | 0.72 | 0.26 | 1.2 |
| Pampa de Tepuel Formation (n = 21) | | | | | | | | | | | | | | | | | | | |
| M1 | 26.72 | 0 | 0 | 0 | 0 | 3.05 | 0 | 5.34 | 15.27 | 0 | 0 | 0 | 24.43 | 0 | 3.05 | 0 | 0 | 22.14 | 0 |
| M3 | 38 | 0 | 5 | 0 | 0 | 13.5 | 0.5 | 11.5 | 0 | 0 | 0 | 0 | 18 | 8 | 0 | 0 | 0 | 0 | 5.5 |
| M5 | 39.02 | 0 | 12.2 | 0 | 0 | 13.82 | 0 | 7.32 | 0 | 0 | 0 | 0 | 26.02 | 0 | 0 | 0 | 1.63 | 0 | 0 |
| M14 | 29.23 | 0 | 6.15 | 0 | 0 | 16.92 | 0 | 10 | 0 | 0 | 0 | 0 | 31.54 | 6.15 | 0 | 0 | 0 | 0 | 0 |
| M17 | 41.18 | 0 | 7.84 | 0.98 | 0.98 | 11.27 | 0.49 | 6.37 | 0.49 | 2.45 | 0.49 | 7.84 | 13.73 | 2.94 | 1.96 | 0 | 0 | 0 | 0.98 |
| M20 | 48.85 | 0 | 1.53 | 0 | 0 | 6.87 | 0 | 3.05 | 1.53 | 0 | 0 | 0 | 36.64 | 0 | 0 | 1.53 | 0 | 0 | 0 |
| M25 | 44.39 | 0 | 2.55 | 0 | 0.51 | 15.82 | 0 | 4.08 | 0.51 | 0.51 | 0 | 1.53 | 26.53 | 1.53 | 0 | 0 | 1.02 | 0 | 1.02 |
| M28 | 24.81 | 0 | 3.76 | 0 | 0 | 6.77 | 0 | 5.26 | 0 | 0 | 0 | 0 | 43.61 | 13.53 | 0 | 0 | 0 | 2.26 | 0 |
| M37 | 34.59 | 0 | 1.5 | 0 | 0 | 5.26 | 0 | 9.77 | 0 | 0 | 0 | 0 | 29.32 | 12.03 | 1.5 | 0 | 6.02 | 0 | 0 |
| M41 | 31.1 | 0 | 1.22 | 0 | 0 | 6.71 | 0 | 6.71 | 3.66 | 0 | 0 | 0 | 42.68 | 6.1 | 0 | 0 | 0 | 0 | 1.83 |

(*continued on next page*)

**Table 2** (*continued*)

| Samples | Qm | Qmi | Qpg | Qpm | Qpf | O | M | P | Lva | Lvm | Lvb | Lvalt | Lml | Lmm-h | Lss | Lsw | Lsf | Lp-Lm | Ac |
|---|---|---|---|---|---|---|---|---|---|---|---|---|---|---|---|---|---|---|---|
| M45 | 37.9 | 0 | 6.45 | 10.48 | 0 | 8.06 | 0 | 12.1 | 0 | 0 | 0 | 0 | 20.97 | 0 | 0 | 0 | 0 | 4.03 | 0 |
| M50 | 52.88 | 0 | 4.33 | 2.4 | 0.48 | 13.46 | 0.48 | 4.81 | 0.96 | 0 | 0 | 0 | 5.77 | 3.85 | 4.81 | 0 | 0 | 4.33 | 1.44 |
| M54 | 53.37 | 0 | 3.85 | 0.48 | 0 | 22.12 | 0 | 7.69 | 0.96 | 3.37 | 0 | 0 | 7.21 | 0.96 | 0 | 0 | 0 | 0 | 0 |
| M55 | 53.02 | 0 | 4.19 | 1.4 | 0 | 10.7 | 1.86 | 3.72 | 2.33 | 0 | 0 | 0 | 20 | 0.93 | 1.86 | 0 | 0 | 0 | 0 |
| M56 | 47.52 | 0.55 | 0.71 | 0 | 0 | 7.8 | 2.84 | 3.55 | 3 | 0 | 0 | 0 | 30.5 | 3.55 | 0 | 0 | 0 | 0 | 0 |
| M69 | 59.61 | 0 | 3.94 | 0.49 | 0 | 18.23 | 0 | 6.4 | 0.99 | 0.49 | 0 | 0 | 9.85 | 0 | 0 | 0 | 0 | 0 | 0 |
| M71 | 42.08 | 0 | 3.47 | 0.5 | 0 | 13.37 | 0 | 6.93 | 0 | 0 | 0 | 0 | 24.75 | 3.96 | 1.98 | 0 | 1.98 | 0 | 0.99 |
| M77 | 40.78 | 0 | 4.85 | 0 | 0 | 6.8 | 0 | 2.43 | 1.46 | 0 | 0 | 0.97 | 33.5 | 7.28 | 0.97 | 0 | 0 | 0.97 | 0 |
| M83 | 52.6 | 0 | 5.84 | 0 | 0 | 12.34 | 0.65 | 2.6 | 0 | 0 | 0 | 0 | 21.43 | 3.25 | 1.3 | 0 | 0 | 0 | 0 |
| M84 | 51.61 | 0 | 1.94 | 2.58 | 0 | 5.16 | 0 | 6.45 | 0 | 0 | 0 | 0 | 26.45 | 1.94 | 3.87 | 0 | 0 | 0 | 0 |
| M87 | 50.39 | 0 | 3.1 | 6.2 | 0 | 14.73 | 3.1 | 8.53 | 0 | 0 | 0 | 0 | 6.98 | 2.33 | 0 | 0 | 3.88 | 0 | 0.08 |
| Average | 42.84 | 0.03 | 4.02 | 1.21 | 0.09 | 11.08 | 0.47 | 6.41 | 1.48 | 0.32 | 0.02 | 0.49 | 23.8 | 3.73 | 1.01 | 0.07 | 0.69 | 1.61 | 0.56 |
| Std dv | 9.59 | 0.12 | 2.69 | 2.52 | 0.24 | 4.86 | 0.92 | 2.74 | 3.26 | 0.86 | 0.1 | 1.69 | 10.7 | 3.8 | 1.41 | 0.33 | 1.53 | 4.77 | 1.23 |
| Valle Chico Formation (n = 17) | | | | | | | | | | | | | | | | | | | |
| VC1 | 17.08 | 2.3 | 4.65 | 0 | 0 | 6.98 | 0 | 0.78 | 30.23 | 0 | 0 | 0 | 0.78 | 0 | 17.05 | 17.83 | 2.33 | 0 | 0 |
| VC2 | 27.33 | 6 | 1.67 | 0 | 0 | 7.5 | 0 | 1.67 | 6.67 | 0.83 | 0 | 6.67 | 0 | 1.97 | 0 | 28.33 | 11.67 | 0 | 0 |
| VC3 | 25 | 6.08 | 0.68 | 0 | 0 | 6.76 | 0 | 0.68 | 2.7 | 0 | 0 | 0 | 0 | 0 | 4.05 | 49.32 | 4.73 | 0 | 0 |
| VC4 | 11.82 | 2 | 0 | 0 | 0 | 3.25 | 0 | 1.63 | 21.95 | 4.88 | 0 | 0 | 4.07 | 0 | 0 | 39.84 | 9.76 | 0.81 | 0 |
| VC4b | 30.19 | 7 | 1.65 | 0 | 0 | 7.44 | 0 | 1.65 | 14.05 | 1.65 | 0 | 0 | 2.48 | 0 | 0 | 26.45 | 5.79 | 0.83 | 0 |
| VC5 | 21.02 | 5.1 | 1.49 | 0 | 0 | 4.48 | 0 | 2.24 | 17.91 | 0 | 0 | 0 | 0 | 0 | 0 | 40.3 | 7.46 | 0 | 0 |
| VC6 | 33.1 | 6 | 5.26 | 0 | 0 | 9.02 | 1.5 | 6.77 | 15.04 | 4.51 | 0 | 0 | 1.5 | 0.75 | 3.76 | 8.27 | 4.51 | 0 | 0 |
| VC7 | 26.16 | 6.4 | 3.88 | 0 | 0 | 0 | 0 | 1.55 | 11.63 | 1.55 | 0 | 0 | 0 | 1.55 | 0 | 38.76 | 8.53 | 0 | 0 |
| VC8 | 38.69 | 9 | 1.54 | 0 | 0 | 10.77 | 0 | 6.15 | 20.77 | 0 | 0 | 0 | 0 | 0 | 3.08 | 3.85 | 3.85 | 2.31 | 0 |
| VC9 | 40 | 10 | 0.78 | 0 | 0 | 10.16 | 0 | 0.78 | 7.81 | 3.12 | 0 | 0 | 7.03 | 0 | 0 | 11.72 | 7.81 | 0.78 | 0 |
| VC10 | 28.2 | 7 | 5.6 | 0.8 | 0 | 8 | 0.8 | 2.4 | 28.8 | 0 | 0 | 0 | 2.4 | 4 | 2.4 | 5.6 | 4 | 0 | 0 |
| VC11 | 28.07 | 7.7 | 1.63 | 0 | 0 | 28.46 | 1.63 | 8.13 | 6.5 | 0 | 0 | 0 | 12.2 | 0 | 1.63 | 0 | 1.63 | 0 | 2.44 |
| VC12 | 29.47 | 7.2 | 3.33 | 0 | 0 | 10 | 0.83 | 11.67 | 14.17 | 0 | 0 | 0 | 4.17 | 0 | 0 | 10 | 9.17 | 0 | 0 |
| VC13 | 36 | 8.5 | 1.67 | 0 | 0 | 17.5 | 0 | 11.67 | 22.5 | 0 | 0 | 0 | 0 | 0 | 0 | 2.5 | 0 | 1.67 | 0 |
| VC14 | 32.74 | 8 | 1.48 | 0 | 0 | 7.41 | 0 | 11.11 | 11.85 | 0 | 0 | 0 | 0 | 0 | 0 | 25.19 | 1.48 | 0 | 0.74 |
| VC15 | 24 | 6 | 0 | 0 | 0 | 5 | 0 | 6.67 | 10 | 3.33 | 0 | 0 | 34.17 | 0 | 0 | 5.83 | 3.33 | 0 | 1.37 |
| VC16 | 22.73 | 5 | 1.68 | 0 | 0 | 5.88 | 0 | 1.638 | 40.34 | 0 | 0 | 0 | 6.72 | 0 | 5.04 | 10.92 | 0 | 0 | 0 |
| Average | 27.74 | 6.43 | 2.18 | 0.05 | 0,00 | 8.74 | 0.28 | 4.54 | 16.64 | 1.17 | 0,00 | 0.39 | 4.44 | 0.49 | 2.18 | 19.1 | 5.06 | 0.38 | 0.27 |
| Std dv | 7.12 | 2.03 | 1.68 | 0.19 | 0,00 | 6.1 | 0.54 | 3.95 | 9.57 | 1.67 | 0,00 | 1.57 | 8.13 | 1.05 | 4.09 | 15.17 | 3.41 | 0.67 | 0.65 |

**Table 3**
Recalculated modal point-count data of the Tepuel Group sandstones.

| | 100% recalculated | | | | Dickinson et al. (1983) | | | | | | | | | |
|---|---|---|---|---|---|---|---|---|---|---|---|---|---|---|
| Samples | Q | F | L | Folk et al. (1970) Classification | Qm | F | L | Qt | F | L | P/F | Lm + Qpm | Lv | Ls |
| Río Genoa Formation (n = 19) | | | | | | | | | | | | | | |
| M130 | 35.04 | 4.33 | 60.63 | Litharenite | 15.35 | 4.33 | 80.32 | 35.04 | 4.33 | 60.63 | 0,00 | 75.59 | 0.79 | 0 |
| M132 | 51.88 | 8.99 | 39.13 | Litharenite | 42.2 | 8.99 | 48.8 | 51.88 | 8.99 | 39.13 | 0.62 | 39.42 | 0 | 0 |
| M132B | 51.72 | 9.65 | 38.63 | Litharenite | 39.31 | 9.65 | 51.03 | 51.72 | 9.65 | 38.63 | 0.08 | 38.1 | 0 | 0 |
| M134 | 61.8 | 18.06 | 20.14 | Feldspathic litharenite | 44.44 | 18.06 | 37.5 | 61.8 | 18.06 | 20.14 | 0.44 | 22.92 | 0 | 0 |
| M136 | 38.89 | 39.58 | 21.52 | Lithic feldsarenite | 31.95 | 39.58 | 28.47 | 38.89 | 39.58 | 21.52 | 0.39 | 21.23 | 0 | 0 |
| M137 | 46.05 | 30.26 | 23.68 | Lithic feldsarenite | 42.76 | 30.26 | 26.98 | 46.05 | 30.26 | 23.68 | 0.59 | 23.23 | 0 | 0 |
| M139 | 42.45 | 32.07 | 25.47 | Lithic feldsarenite | 37.26 | 32.07 | 30.66 | 42.45 | 32.07 | 25.47 | 1.83 | 24.05 | 0 | 2.36 |
| M141 | 35.3 | 49.99 | 14.71 | Feldsarenite | 30.59 | 49.99 | 19.41 | 35.3 | 49.99 | 14.71 | 0.49 | 14.37 | 0 | 0 |
| M143 | 35.99 | 36.16 | 27.84 | Lithic feldsarenite | 33.12 | 36.17 | 30.72 | 35.99 | 36.16 | 27.84 | 0.15 | 27.27 | 0.48 | 0 |
| M145 | 35.59 | 12.5 | 51.91 | Litharenite | 28.37 | 12.5 | 59.13 | 35.59 | 12.5 | 51.91 | 0.86 | 53.37 | 0.96 | 0.96 |
| M147 | 46.12 | 14.56 | 39.32 | Feldspathic litharenite | 30,58 | 14.56 | 54.85 | 46.12 | 14.56 | 39.32 | 0.25 | 34.95 | 0 | 4.37 |
| M148 | 32.15 | 18.83 | 49.02 | Feldspathic litharenite | 27.55 | 18.83 | 53.61 | 32.15 | 18.83 | 49.02 | 0.32 | 48.41 | 0.8 | 0 |
| M149 | 44.28 | 13.33 | 42.38 | Litharenite | 36.66 | 13.33 | 50,00 | 44.28 | 13.33 | 42.38 | 0.33 | 44.08 | 0.47 | 0 |
| M151 | 34.03 | 48.61 | 17.34 | Lithic feldsarenite | 29.86 | 48.61 | 21.53 | 34.03 | 48.61 | 17.34 | 0.71 | 15.75 | 0 | 1.37 |
| M152 | 74.77 | 7.47 | 17.76 | Feldspathic litharenite | 64.24 | 7.47 | 28.29 | 74.77 | 7.47 | 17.76 | 0.17 | 16.23 | 0.44 | 2.625 |
| M153 | 44.1 | 23.08 | 32.82 | Feldspathic litharenite | 36.91 | 23.08 | 40,00 | 44.1 | 23.08 | 32.82 | 0.96 | 35.03 | 0 | 0.51 |
| M155 | 29.95 | 25.12 | 44.92 | Feldspathic litharenite | 26.57 | 25.12 | 48.3 | 29.95 | 25.12 | 44.92 | 0.79 | 45.89 | 0 | 0.48 |
| M157 | 33.66 | 28.22 | 38.11 | Feldspathic litharenite | 28.21 | 28.22 | 43.56 | 33.66 | 28.22 | 38.11 | 0.43 | 38.12 | 0 | 0 |
| M163 | 36.41 | 38.07 | 25.52 | Lithic feldsarenite | 30.13 | 38.07 | 31.79 | 36.41 | 38.07 | 25.52 | 0.78 | 23.43 | 2.09 | 0 |
| Average | 42.64 | 24.15 | 33.2 | | 34.53 | 24.15 | 41.32 | 42.64 | 24.15 | 33.2 | 0.54 | 33.76 | 0.32 | 0.67 |
| Std dv | 10.95 | 13.54 | 12.73 | | 9.69 | 13.54 | 14.86 | 10.95 | 13.54 | 12.73 | 0.41 | 15.06 | 0.53 | 1.12 |
| Mojón de Hierro Formation (n = 18) | | | | | | | | | | | | | | |
| M61 | 80.32 | 5.17 | 14.5 | Sublitharenite | 69.95 | 5.18 | 24.87 | 80.32 | 5.17 | 14.5 | 0.25 | 16.49 | 4.64 | 0 |
| M62 | 79.5 | 5.5 | 15 | Sublitharenite | 66 | 5.5 | 28.5 | 79.5 | 5.5 | 15 | 2.67 | 17.5 | 6.5 | 1 |
| M63 | 73.15 | 2.78 | 24.07 | Litharenite | 44.91 | 2.78 | 52.31 | 73.15 | 2.78 | 24.07 | 1.99 | 42.59 | 0 | 0 |
| M66 | 59.39 | 9.78 | 30.83 | Litharenite | 52.62 | 9.78 | 37.6 | 59.39 | 9.78 | 30.83 | 1.6 | 26.32 | 2.26 | 2.26 |
| M68 | 53.06 | 14.96 | 31.98 | Feldspathic litharenite | 46.26 | 14.96 | 38.78 | 53.06 | 14.96 | 31.98 | 1.44 | 31.98 | 0 | 0 |
| M89 | 29.85 | 8.46 | 61.69 | Litharenite | 27.86 | 8.46 | 63.68 | 29.85 | 8.46 | 61.69 | 1.13 | 61.7 | 0 | 0 |
| M90 | 39.68 | 18.11 | 42.21 | Feldspathic litharenite | 35.33 | 18.11 | 46.56 | 39.68 | 18.11 | 42.21 | 1.5 | 22.47 | 19.74 | 0 |
| M93 | 63.42 | 14.82 | 21.76 | Feldspathic litharenite | 46.3 | 14.82 | 38.89 | 63.42 | 14.82 | 21.76 | 0.39 | 28.7 | 0 | 0 |
| M94 | 54.54 | 8.09 | 37.37 | Litharenite | 44.44 | 8.09 | 47.47 | 54.54 | 8.09 | 37.37 | 0.78 | 43.43 | 0 | 0 |
| M95 | 52.15 | 23.2 | 24.65 | Feldspathic litharenite | 47.32 | 23.2 | 29.48 | 52.15 | 23.2 | 24.65 | 0.23 | 22.71 | 1.93 | 0 |
| M99 | 67.15 | 9.28 | 23.57 | Feldspathic litharenite | 60.72 | 9.28 | 30 | 67.15 | 9.28 | 23.57 | 1.6 | 27.14 | 0 | 0 |
| M104 | 85.27 | 5.43 | 9.3 | Sublitharenite | 72.09 | 5.43 | 22.48 | 85.27 | 5.43 | 9.3 | 0.4 | 20.93 | 0 | 0 |
| M108 | 73.34 | 5.92 | 20.74 | Litharenite | 61.48 | 5.92 | 32.6 | 73.34 | 5.92 | 20.74 | 0.33 | 18.52 | 0 | 2.22 |
| M111 | 63.31 | 20.11 | 16.58 | Lithic feldsarenite | 58.79 | 20.11 | 21.1 | 63.31 | 20.11 | 16.58 | 0.18 | 11.55 | 4.02 | 3.02 |
| M112 | 53.04 | 25.97 | 20.99 | Lithic feldsarenite | 48.62 | 25.97 | 25.41 | 53.04 | 25.97 | 20.99 | 0.42 | 21.99 | 0.52 | 0 |
| M122 | 69.15 | 14.02 | 16.83 | Feldspathic litharenite | 60.74 | 14.02 | 25.24 | 69.15 | 14.02 | 16.83 | 0.11 | 18.23 | 0 | 0 |
| M126 | 31.82 | 6.82 | 61.36 | Litharenite | 31.82 | 6.82 | 61.36 | 31.82 | 6.82 | 61.36 | 0.5 | 61.37 | 0 | 0 |
| M129 | 67.69 | 3.08 | 29.23 | Litharenite | 61.54 | 3.08 | 35.38 | 67.69 | 3.08 | 29.23 | 0.33 | 28.46 | 0.77 | 0 |
| Average | 60.88 | 11.19 | 27.93 | | 52.04 | 11.19 | 36.76 | 60.88 | 11.19 | 27.93 | 0.88 | 29,00 | 2.24 | 0.47 |
| Std dv | 15.44 | 6.8 | 14.35 | | 12.42 | 6.8 | 12.54 | 15.44 | 6.8 | 14.35 | 0.78 | 14.03 | 4.65 | 0.95 |
| Pampa Tepuel Formation (n = 21) | | | | | | | | | | | | | | |
| M1 | 26.72 | 8.39 | 64.89 | Litharenite | 26.72 | 8.39 | 64.89 | 26.72 | 8.39 | 64.89 | 1.75 | 46.57 | 15.27 | 3.05 |
| M3 | 45.50 | 26.98 | 27.51 | Feldspathic litharenite | 40.21 | 26.98 | 32.80 | 45.50 | 26.98 | 27.51 | 0.82 | 26 | 0 | 0 |
| M5 | 51.21 | 21.14 | 27.65 | Feldspathic litharenite | 39.02 | 21.14 | 39.85 | 51.21 | 21.14 | 27.65 | 0.53 | 26.02 | 0 | 1.63 |
| M14 | 35.38 | 26.92 | 37.69 | Feldspathic litharenite | 29.23 | 26.92 | 43.84 | 35.38 | 26.92 | 37.69 | 0.59 | 37.69 | 0 | 0 |
| M17 | 51.49 | 18.31 | 30.2 | Feldspathic litharenite | 41.59 | 18.31 | 40.1 | 51.49 | 18.31 | 30.2 | 0.54 | 17.65 | 11.27 | 1.96 |
| M20 | 50.38 | 9.92 | 39.7 | Litharenite | 48.11 | 9.77 | 42.12 | 50.38 | 9.92 | 39.7 | 0.44 | 36.64 | 1.53 | 1.53 |
| M25 | 47.94 | 20.11 | 31.96 | Feldspathic litharenite | 44.85 | 20.11 | 35.05 | 47.94 | 20.11 | 31.96 | 0.26 | 28.06 | 2.55 | 1.02 |
| M28 | 28.57 | 12.03 | 59.4 | Litharenite | 24.81 | 12.03 | 63.16 | 28.57 | 12.03 | 59.4 | 0.78 | 59.4 | 0 | 0 |
| M37 | 36.09 | 15.03 | 48.87 | Litharenite | 34.59 | 15.03 | 50.38 | 36.09 | 15.03 | 48.87 | 1.86 | 41.35 | 0 | 7.52 |
| M41 | 32.92 | 13.67 | 53.41 | Litharenite | 31.68 | 13.67 | 54.65 | 32.92 | 13.67 | 53.41 | 1 | 48.78 | 3.66 | 0 |
| M45 | 54.84 | 20.16 | 25.00 | Feldspathic litharenite | 37.90 | 20.16 | 41.93 | 54.84 | 20.16 | 25.00 | 1.50 | 35.48 | 0 | 0 |
| M50 | 60.97 | 19.02 | 20.01 | Feldspathic litharenite | 53.65 | 19.02 | 27.32 | 60.97 | 19.02 | 20.01 | 0.35 | 16.35 | 0.96 | 4.81 |
| M54 | 57.69 | 29.81 | 12.5 | Lithic feldsarenite | 53.36 | 29.81 | 16.83 | 57.69 | 29.81 | 12.5 | 0.35 | 8.65 | 4.33 | 0 |
| M55 | 58.60 | 16.28 | 25.12 | Feldspathic litharenite | 53.01 | 16.28 | 30.71 | 58.60 | 16.28 | 25.12 | 0.3 | 22.33 | 2.33 | 1.86 |
| M56 | 48.77 | 14.19 | 37.04 | Feldspathic litharenite | 48.06 | 14.19 | 37.75 | 48.77 | 14.19 | 37.04 | 0.33 | 34.05 | 3 | 0 |
| M69 | 64.04 | 24.63 | 11.33 | Lithic feldsarenite | 59.61 | 24.63 | 15.76 | 64.04 | 24.63 | 11.33 | 0.35 | 10.34 | 1.48 | 0 |
| M71 | 46.51 | 20.50 | 32.99 | Feldspathic litharenite | 42.5 | 20.50 | 37.00 | 46.51 | 20.50 | 32.99 | 0.52 | 29.21 | 0 | 3.96 |
| M77 | 45.63 | 9.23 | 45.15 | Litharenite | 40.78 | 9.23 | 49.99 | 45.63 | 9.23 | 45.15 | 0.36 | 41.75 | 2.43 | 0.97 |
| M83 | 58.43 | 15.59 | 25.98 | Feldspathic litharenite | 52.59 | 15.59 | 31.82 | 58.43 | 15.59 | 25.98 | 0.20 | 24.68 | 0 | 1.3 |
| M84 | 56.13 | 11.61 | 32.26 | Feldspathic litharenite | 51.61 | 11.61 | 36.78 | 56.13 | 11.61 | 32.26 | 1.25 | 30.97 | 0 | 3.87 |
| M87 | 60.15 | 26.56 | 13.29 | Lithic feldsarenite | 50.78 | 26.56 | 22.66 | 60.15 | 26.56 | 13.29 | 0.48 | 15.51 | 0 | 3.88 |
| Average | 49.69 | 17.98 | 32.33 | | 44.37 | 17.97 | 37.65 | 49.69 | 17.98 | 32.33 | 0.69 | 30.36 | 2.32 | 1.78 |
| Std dv | 10.22 | 5.88 | 13.36 | | 9.42 | 5.89 | 12.18 | 10.22 | 5.88 | 13.36 | 0.48 | 12.76 | 3.85 | 2.0 |
| Valle Chico Formation (n = 17) | | | | | | | | | | | | | | |
| VC1 | 24.03 | 7.76 | 68.2 | Litharenite | 19.38 | 7.76 | 72.86 | 24.03 | 7.76 | 68.2 | 0.11 | 0.78 | 30.23 | 37.21 |
| VC2 | 34.9 | 9.14 | 55.97 | Litharenite | 33.23 | 9.14 | 57.63 | 34.9 | 9.14 | 55.97 | 0.22 | 1.97 | 14.17 | 40 |
| VC3 | 31.76 | 7.44 | 60.8 | Litharenite | 31.08 | 7.44 | 61.48 | 31.76 | 7.44 | 60.8 | 0.1 | 0 | 2.7 | 58.1 |
| VC4 | 13.82 | 4.88 | 81.3 | Litharenite | 13.82 | 4.88 | 81.3 | 13.82 | 4.88 | 81.3 | 0.5 | 4.88 | 26.83 | 49.6 |
| VC4b | 39.16 | 9.17 | 51.67 | Litharenite | 37.5 | 9.17 | 53.34 | 39.16 | 9.17 | 51.67 | 0.22 | 3.31 | 15.7 | 32.24 |

(*continued on next page*)

**Table 3** (*continued*)

| | 100% recalculated | | | | Dickinson et al. (1983) | | | | | | | | | |
|---|---|---|---|---|---|---|---|---|---|---|---|---|---|---|
| Samples | Q | F | L | Folk et al. (1970) Classification | Qm | F | L | Qt | F | L | P/F | Lm + Qpm | Lv | Ls |
| VC5 | 27.61 | 6.72 | 65.67 | Litharenite | 26.12 | 6.72 | 67.16 | 27.61 | 6.72 | 65.67 | 0.5 | 0 | 17.91 | 47.76 |
| VC6 | 44.36 | 17.29 | 38.34 | Feldspathic litharenite | 39.1 | 17.29 | 43.60 | 44.36 | 17.29 | 38.34 | 0.64 | 2.25 | 19.55 | 16.54 |
| VC7 | 36.44 | 1.55 | 62.01 | Litharenite | 32.56 | 1.55 | 65.89 | 36.44 | 1.55 | 62.01 | 0 | 1.55 | 13.18 | 47.29 |
| VC8 | 49.23 | 16.92 | 33.86 | Feldspathic litharenite | 47.68 | 16.92 | 35.4 | 49.23 | 16.92 | 33.86 | 0.57 | 2.31 | 20.77 | 10.78 |
| VC9 | 50.79 | 10.94 | 38.27 | Litharenite | 50 | 10.94 | 39.05 | 50.79 | 10.94 | 38.27 | 0.07 | 7.81 | 10.93 | 19.53 |
| VC10 | 41.6 | 11.2 | 47.2 | Litharenite | 35.2 | 11.2 | 53.6 | 41.6 | 11.2 | 47.2 | 0.27 | 7.2 | 28.8 | 12 |
| VC11 | 38.33 | 39.17 | 22.5 | Lithic feldsarenite | 36.66 | 39.17 | 24.18 | 38.33 | 39.17 | 22.5 | 0.27 | 12.2 | 6.5 | 3.26 |
| VC12 | 39.99 | 22.5 | 37.51 | Feldspathic litharenite | 36.67 | 22.45 | 40.84 | 39.99 | 22.5 | 37.51 | 1.08 | 4.17 | 14.17 | 19.17 |
| VC13 | 45.26 | 28.6 | 26.14 | Lithic feldsarenite | 43.62 | 28.6 | 27.78 | 45.26 | 28.6 | 26.14 | 0.67 | 1.67 | 22.5 | 2.5 |
| VC14 | 42.53 | 18.66 | 38.81 | Feldspathic litharenite | 41.04 | 18.66 | 40.3 | 42.53 | 18.66 | 38.81 | 1.5 | 0 | 11.85 | 26.67 |
| VC15 | 30.51 | 11.87 | 57.62 | Litharenite | 30.51 | 11.87 | 57.62 | 30.51 | 11.87 | 57.62 | 1.33 | 34.17 | 13.33 | 9.16 |
| VC16 | 29.43 | 7.522 | 63.05 | Litharenite | 27.74 | 7.52 | 64.73 | 29.43 | 7.522 | 63.05 | 0.28 | 6.72 | 40.34 | 15.96 |
| Average | 35,00 | 13.18 | 47.91 | | 32.85 | 13.18 | 49.94 | 35,00 | 13.18 | 47.91 | 0.49 | 5.35 | 18.2 | 26.34 |
| Std dv | 10.8 | 9.12 | 17.47 | | 10.45 | 9.12 | 17.77 | 10.8 | 9.12 | 17.47 | 0.43 | 7.9 | 9.1 | 17.03 |

kaolinite cement are extremely scarce, as prevailing cements are rim cement of chlorite and pore-filling cement of microquartz and calcite.

All the analyzed sandstones in the Tepuel-Genoa Basin show a high degree of mechanical, and in some cases chemical, compaction. Concavo-convex and frequently sutured contacts are dominant, while discrete amounts of long contacts also occur. The principal effect of the mechanical compaction over ductile grains was the diagenetic deformation of schists clasts, and rarely the formation of pseudomatrix from some slate and mudstone grains. In most cases, pseudomatrix can be assigned to the original clast, and when it was not possible, the questionable grains were counted as undetermined clast. In sandstones of the Río de Genoa Formation, some feldspars exhibit displacement of the twin lamellae by compaction (Fig. 8e).

Optical porosity is very low in the sandstones (lower than 2%), as that primary porosity is extremely low. Secondary porosity results from feldspar clasts dissolution, including both K-feldspar and plagioclase (Fig. 8f), or partial dissolution of clay cement. In the case of dissolution of feldspar grains, usually, grains were not wholly dissolved, preserving remains of the original clasts (Fig. 8f); in these cases, the pore space was assigned to feldspar during the point counts. Very rarely secondary porosity results from massive dissolution of grains.

Different from feldspar grain dissolution that forms mesopores and macropores (using the scale of Limarino et al., 2020b), dissolution of clay cement, or more rarely calcite cement, produced mainly microporosity whereby its origin can be easily determined. This process does not impact on detrital modes of the sandstones.

## 6. Potential provenance areas

The diagrams of Dickinson et al. (1983) and Dickinson (1985) were used as a first approximation to identify sandstone source areas. In the case of the QmFLt triangle, most samples plot in the recycled orogen field (mainly intermediate and quartzose) while some samples plot in the dissected volcanic arc field (Fig. 9a). A similar situation occurs in the second triangle (QtFLi, Fig. 9b), but some samples also plot in the transitional arc field.

It is important to note that the samples included in the volcanic arc fields correspond to sandstones from the Río Genoa Formation, which exhibits very low percentages of volcanic grains, but instead have lithic grains dominated by metamorphic clasts. On the other hand, the samples belonging to the Valle Chico Formation, which bears abundant volcanic fragments, are located in the recycled orogeny field (Fig. 9a and b).

This apparent contradiction is understood when the existence of different provenance areas for the Tepuel Group are considered. In these cases, Dickinson's diagrams should be used as a first approach for identifying sandstone provenance, but when sand comes from different areas, petrofacies recognition, and the identification of key components, become necessary for unraveling the various provenance sources (Net and Limarino, 2006; Limarino and Giordano, 2016).

The provenance study of the Tepuel Group was approached considering the potential areas of provenance. According to regional information, three main areas should be taken into account: 1. The crystalline basement of the Deseado Massif, 2. Early-middle Paleozoic, partially metamorphosed, sedimentary successions, and 3. The Devonian-Carboniferous volcanic arc. This last provenance comprises two different volcanic chains, the "western volcanic arc" postulated by Ramos (2008), and the magmatic arcs described in Chile by Hervé et al. (2016) formed during the Devonian and the Early Carboniferous (Fig. 2).

Derivation of sands from the Deseado Massif basement should include fragments of crystalline rocks (schists, gneisses, and granitoids), the monomineralic clasts derived from the erosion of these rocks, and some metaquartzites. Although different compositions of clasts could be derivated from this terrain, the index of Deseado Massif provenance here considered includes grains of polycrystalline quartz exhibiting cataclastic texture (Qpm), microcline (M), different types of schist (Lmm-h), and granitoids (Lp-Lm).

Partially metamorphosed sedimentary successions comprise two different areas. On the one hand, those linked to the Deseado Massiff represented in the La Modesta Formation (Moreira et al., 2005) and the pre-Carboniferous strata of the Cushamen Formation (Marcos et al., 2018). On the other hand, the western accretionary complex (mainly developed in Chile) could have supplied metasedimentary grains to the Tepuel Basin. In both cases, key clasts correspond to slates, mudstones, wackes, and quartzarenites (probably partially metamorphosed).

The existence of a late Paleozoic volcanic arc was raised by Ramos (2008) interpreting the Tepuel-Genoa Basin as a forearc basin. Therefore, the identification of volcanic supply becomes critical, not only for reconstructing provenance areas but also for testing hypotheses on the geodynamic interpretation of Patagonia. The key clasts that would indicate provenance from volcanic terrains correspond to different types of volcanic grains (Lva, Lvm, Lvb, in Table 1).

Monocrystalline quartz grains are essential for defining various petrofacies because their percentages can be used for separating crystalline basement rocks from grains coming from a volcanic arc. The monocrystalline quartz grains can also serve to identify derivation from sedimentary rocks, especially in quartz-rich sandstones. For identifying quartz grains derived unquestionably from volcanic areas, the quartz clasts show idiomorph crystals, vitric inclusions, or embayed edges (Qmi, Table 1). The volcanic quartz grains can easily be separated from those exhibiting rounded to subrounded shapes, without embayment, lacking vitric inclusions, or any other evidence of volcanic derivation (Qm, Table 1).

The joint analysis of the detrital modes (Tables 2 and 3) and the potential provenance areas (Fig. 2), allows defining seven modal components with discriminant value for identifying provenance areas (Qm, Qi, Lv, Lmm-h, Lm-Lp, Lm, Qpm). Despite feldspar being a

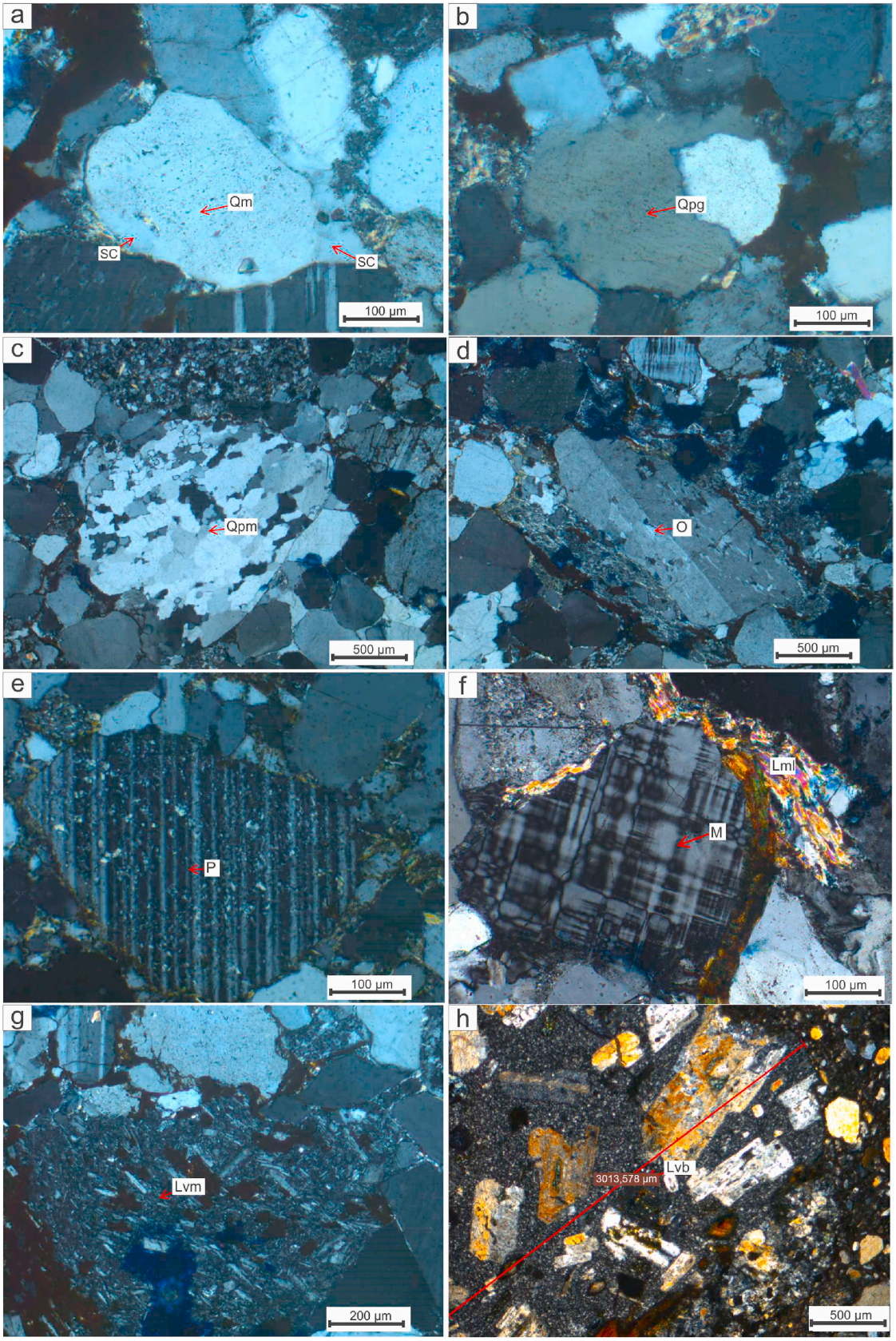


**Fig. 5.** Main modal components recognized during the counted-point in the sandstones of the Tepuel Group, a. monocrystalline clasts (Qm) exhibiting siliceous cement (SC), b. polycrystalline quartz grain (Qpg), c. polycrystalline quartz with cataclastic texture (Qpm), d. twinned crystal of orthoclase (O), e. clast of plagioclase showing polysynthetic twinning (P), f. microcline exhibiting the characteristic chessboard twinning (M), g. aphyric volcanic clast with microlitic groundmass (Lvm) and h. volcanic fragments showing lathwork texture (Lvb).

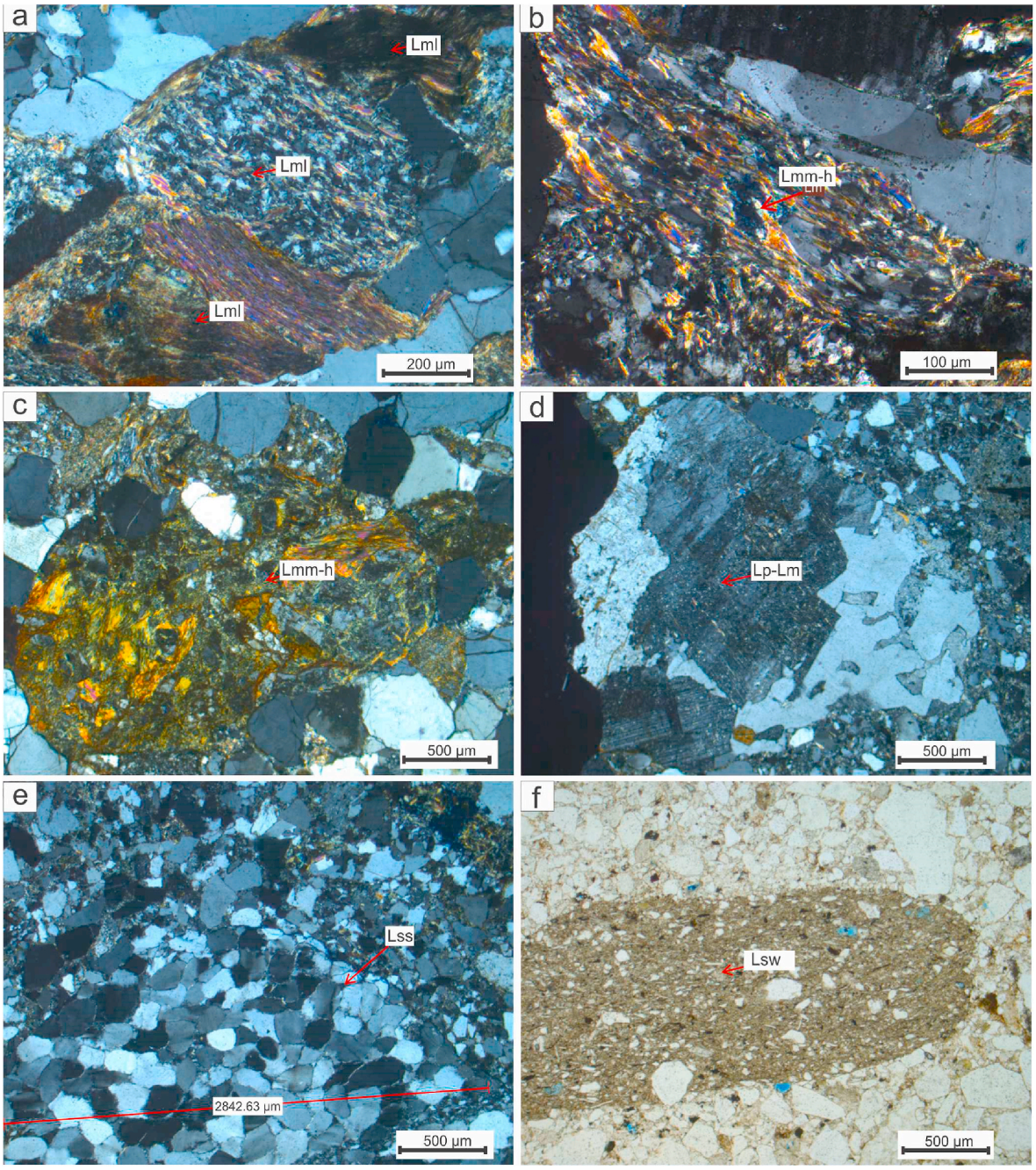


**Fig. 6.** Main modal components in the Tepuel Group sandstones, a. low-grade metamorphic clast (Lml), b and c. medium to high-grade metamorphic fragment, d. clast of fine-grained granitois (aplite? Lp-Lm), e and f. examples of sandstone clasts with low (e, Lss) and high (f, Lsw) amount of matrix.

quantitatively important component in the sandstones, both k-feldspar (orthoclase) and plagioclase have no significant differences in the samples, and their assignment to a specific provenance area is uncertain. Only the microcline grains are unquestionable, as they indicate derivation from crystalline acidic rocks, but its percentage in the studied sandstones is very low (Table 2).

Using the seven discriminant modal components discussed above, three petrofacies were recognized: 1. Quartzose-lithic ($Qm_{69}Lv_2Lm_{29}$), 2. Quartzose ($Qm_{89}Lv_4Lm_7$) and 3. Volcanic-sedimentary ($Qm_{60}Lv_{38}Lm_1$, Fig. 10). Table 4 shows the recalculated modes (normalized to 100%) for the sandstones in each formation.

## 7. Petrofacies description

### 7.1. Quartzose-lithic petrofacies (21 samples) ($Qm_{69}Lv_2Lm_{29}$)

This petrofacies contains the highest amount of high-to medium-grade metamorphic clasts together with some plutonic fragments (mainly aplites) clasts (Table 4). The amount of metamorphic and granitic clasts ranges from 20% to 76%. Besides, this petrofacies contains the lowest proportions of volcanic fragments (less than 2%).

The main component is monocrystalline quartz, which varies from 25% to 84% (69% on average). Quartz grains are rounded to sub-rounded in shape and frequently show fluid inclusions, and in some cases, inclusions of acicular minerals (rutile, zircon); clasts with symplectite textures also occur. Although flashy extinction predominates,

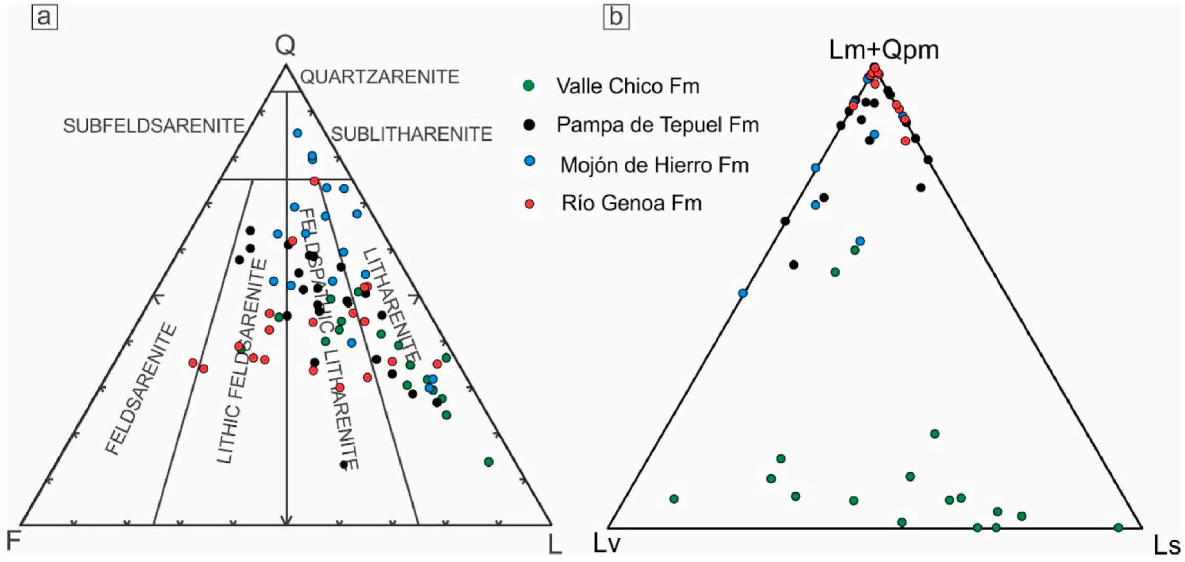


**Fig. 7.** a. sandstone composition in the classification of Folk et al. (1970), observe the predominance of litharenites and feldspathic litharenites, with the sublitharenites and feldsarenites being very scarce, b: triangular diagram separating metamorphic + mylonite (Lm + Qpm), volcanic (Lv) and sedimentary (Ls) clasts, note that the sandstones belonging to the Valle Chico Formation are separated from the rest of the sandstones.

some quartz clasts show undulose extinction.

Metamorphic clasts (29% on average) consist of micaceous schists, amphibolites, fine-grained quartz-micaceous schists, and gneisses. Micaceous schists form more than half of the metamorphic grains; they are mainly composed of muscovite schist and less frequently biotite schist showing lepidoblastic textures. Amphibole schist and quartz-micaceous schist are rare; the first type is dominated by hornblende, while the second is formed by equigranular quartz grains intergrowing with flaky muscovite or biotite crystals.

Regarding rare coarse-grained metamorphic and plutonic grains, grains of gneisses are composed of quartz, feldspar, biotite, and muscovite, showing lepidoblastic and granoblastic textures. Plutonic fragments occur as fine-grained granitoids (aplites) composed of quartz, K-feldspar, and plagioclase together with a lesser amount of micaceous minerals (biotite or muscovite). In these fragments, schistosity is missing.

Volcanic clasts and quartz grains indicating volcanic derivation (bearing negative crystals or embayed edges) are extremely scarce and are indeed absent in many samples. The few volcanic fragments that do occur mainly show acidic compositions with aphyric felsitic texture and partial alteration to clay minerals.

Outside the key components, K-feldspar (mainly orthoclase) prevails over plagioclase in most of the samples (P/F ratio 0.8 on average), and the number of sandstones and mudstones grains are scarce (less than 1%). Another complementary feature of this petrofacies is the low, but significant percentage of accessory minerals, principally biotite and muscovite, together with traces of amphibole. Although quantitatively these minerals are not relevant, the fact that they are almost absent in the other two petrofacies must be noted.

### 7.2. *Quartzose petrofacies (36 samples) ($Qm_{89}Lv_4Lm_7$)*

The Quartzose petrofacies is characterized by a low percentage of metamorphic clasts (7%), the highest proportions of Qm type quartz (89%), and very low percentages of volcanic fragments (4%, including quartz derived from volcanic rocks).

Quartz Qm type shows similar features to similar grain types in the quartzose-lithic petrofacies and is characterized by the presence of rounded to well-rounded grains, which show flashy and undulate extinction and rarely contain acicular mineral inclusions.

Metamorphic clasts include different types of schists (from micaceous to quartz-micaceous) and very scarce fragments of gneisses and granitoids.

Regarding volcanic clasts, sandstones in this petrofacies exhibit a small increase in these grains when compared with the quartzose-lithic petrofacies, as well as a broader composition since they occur as not only volcanic clasts of acidic composition, but also as intermediate volcanic grains that can be assigned to andesites.

Similar to the previously considered petrofacies, the average ratio of K-feldspar/plagioclase is less than 1, and the percentages of sandstone and mudstone grains show a slight increase in abundance.

### 7.3. *Volcanic-sedimentary petrofacies (18 samples) ($Qm_{60}Lv_{38}Lm_1$)*

This petrofacies is characterized by an increase in the proportion of volcanic fragments, the lowest percentages of quartz, and the extremely low values of medium- and high-grade metamorphic grains.

Two types of volcanic fragments are recognized. The first type consists of acidic (rhyolites to dacites) grains, which exhibit aphanitic texture, and rare microporphyric grains with felsitic and granophyric groundmass. In the case of microporphyric texture, phenocrysts are mainly fresh to highly altered, twinned plagioclase grains, some of which show a sieve-like texture.

The second type of volcanic grains is less common and consists of intermediate volcanic rock fragments (andesite to trachytes), exhibiting aphanitic textures with pilotaxitic and bostonitic groundmass. Volcanic fragments of basic composition are extremely rare.

Sandstone, mudstone, and slate clasts (up to 40%, 19% on average) frequently display ductile deformation that occurred during diagenesis, which favored the development of a pseudomatrix. Several of these fragments show imperfect development of schistosity for which the presence of a low-grade of metamorphism cannot be ruled out. Some sandstones grains show similar features to the lepto-metamorphosed sandstones exposed in the nearby outcrops of the Arroyo Pescado Formation.

There are two principal types of quartz fragments: 1) rounded to subrounded monocrystalline quartz (Qm in Tables 1), and 2) monocrystalline quartz showing idiomorph shape, negative crystals, sieve textures and embayed edges (Qmi in Table 1). Establishing the derivation of the first type (Qm) is uncertain since it may have been supplied by crystalline, sedimentary, or even volcanic sources. In contrast, the Qmi type unquestionably exhibits a volcanic origin, and the idiomorph

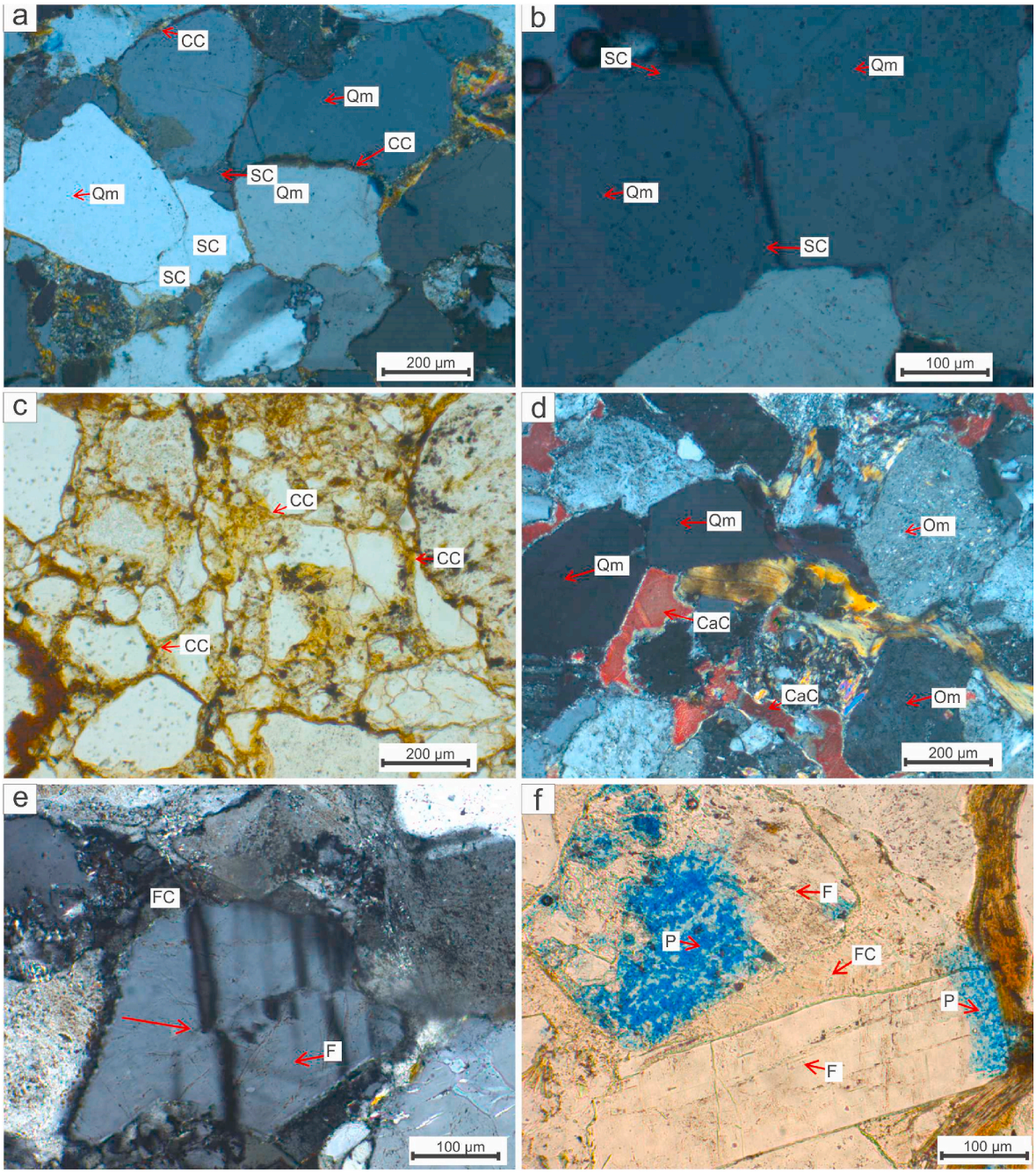


**Fig. 8.** Main diagenetic features of the Tepuel Group sandstones, a. siliceous cement (SC) as overgrowths as megaquarzt; b. detail of siliceous overgrowths (SC) around monocrystalline quartz (Qm); c. rim cement of chlorite-illite (CC); d. calcite cement (CaC) as pore-filling intergranular cement; e. feldspar cement (FC) and displacement of twin lamellae of feldspar (F) by compaction (arrow) and f. secondary porosity (P) by partial dissolution of feldspars (F) and feldspar cement (FC).

shapes of many clasts suggest a short transport distance.

Fragments of high- and medium-grade metamorphic rocks are scarce and consist of mica-schists and some gneiss-like clasts.

## 8. Petrofacies: validity and significance

The composition of the described petrofacies appears in the triangular diagram of Fig. 11, where three sets of samples are defined. The supply of volcanic and sedimentary terrains (volcanic sedimentary petrofacies) corresponds to the lower-left part of the diagram (green points, Fig. 11) characterized by having more than 30% of volcanic fragments, monocrystalline idiomorphic quartz, and very fine-grained immature sandstones.

The major part of the samples is along the right axis of the diagram, which is divided into two groups. On the one hand, the sandstones that exhibit more than 25% of clasts derived from crystalline rocks (red points in Fig. 11), including gneisses, migmatites, granitoids, and polycrystalline quartz with cataclastic texture (mylonites). These samples correspond to the quartzose-lithic petrofacies. On the other hand, those sandstones showing enrichment in monocrystalline quartz without the characteristic textures of derivation from volcanic rocks (black points in Fig. 11) correspond to quartzose petrofacies. These sandstones probably depict the supply from sedimentary terrains coupled with a minor contribution of crystalline rocks derivation.

For establishing the validity of the three petrofacies, we used the Principal Component Analysis methodology applied to the study of

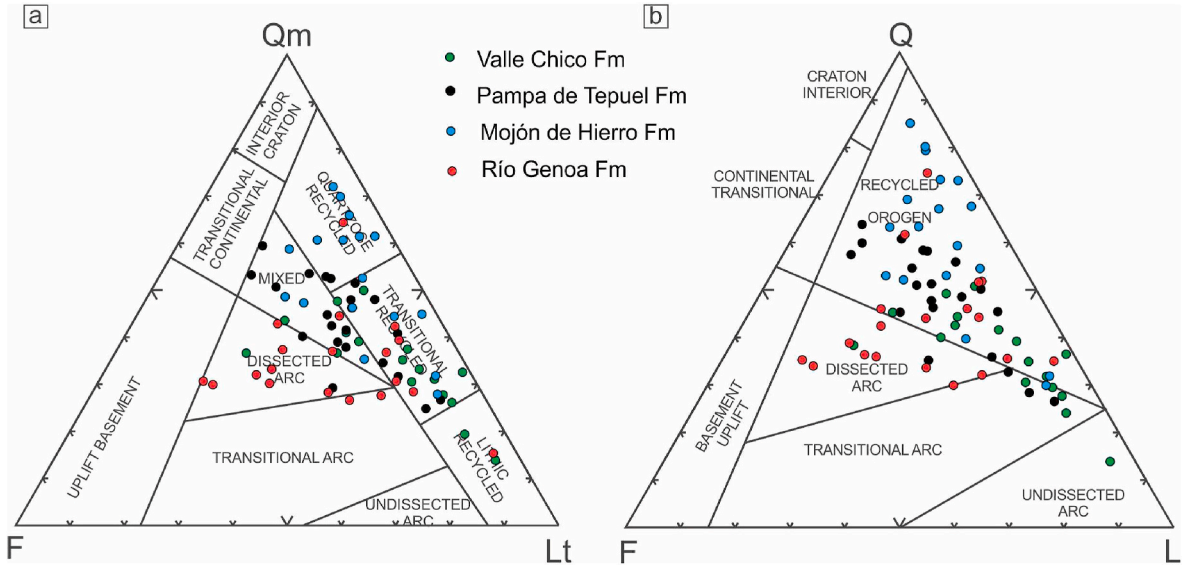


**Fig. 9.** a. QmFL and b. QFL ternary diagrams of Dickinson et al. (1983).

| PETROFACIES | KEY | INTERPRETATION |
|---|---|---|
| Volcanic-sedimentary | Lv+Lsw+Qmi > 30% | Signal of volcanic and sedimentary supply including inmature sandstones and lepto-metamorphic grains. |
| | Lv+Lsw+Qmi < 30% | |
| Quartzose-lithic | Lmm-h+(Lm-Lp)+Qpm > 25% | Signal of crystalline basement |
| Quartzose | Lmh+(Lm-Lp)+Qpm < 25% | Signal of sedimentary terrains with minor contribution of crystalline basement |

**Fig. 10.** Petrofacies recognized and their interpretation.

detrital modes in sandstones (Weltje, 2002; Sidgel and Sakay, 2013; Limarino and Giordano, 2016). The employed modal components were: Qm, Qmi, Lv, Lsw, Qm, Lss, Lmh, Lm-Lp, Qpm (Table 1). The biplot data using PAST 3.07 software shows a good separation among the three petrofacies and confirms that at least three sets can be identified using the modal composition of the sampled sandstones (Fig. 12).

The quartzose-lithic petrofacies is characterized by the predominance of monocrystalline quartz grains (Qm, excluding those derived from volcanic sources) and has the highest values of metamorphic rocks fragments, including mylonites, of the three sandstone petrofacies and contains a significant amount of feldspar (Fig. 10). This detrital association is interpreted as derived from basement rocks that included low-to high-grade metamorphic rocks (Lmm-h), highly deformed granites, gneisses (Lp-Lm, Qpm) and probably some granitoids (Mm). From the regional point of view, the lithological assemblage listed above occurs in the basement rocks of the Deseado Massif, which is here considered as the main provenance area for the quartzose-lithic petrofacies (Figs. 2 and 10). Regarding the quartzose petrofacies, it is dominated by monocrystalline quartz grains (89% on average) with minor contributions of metamorphic grains and extremely scarce volcanic fragments (Fig. 10). The abundance of monocrystalline quartz, frequently showing well-rounded shapes, suggests that sand grains could have suffered prolonged transport or multiple cycles of erosion and deposition. In this interpretation, the clasts correspond to the reworking of previous sedimentary units that covered the crystalline basement, or possibly to the erosion of quartzites that form part of the Deseado Massif basement (Fig. 10).

Concerning the volcanic-sedimentary petrofacies (Fig. 10), its principal feature is the abundance of acidic and mesosilicic volcanic rocks fragments, sedimentary clasts, and the presence of quartz grains derived from the erosion of volcanic rocks (Qmi). Moreover, as opposed to the quartzose-lithic petrofacies, fragments of wackes and mudstones are common in the volcanic-sedimentary petrofacies.

The composition of clasts in the volcanic-sedimentary petrofacies suggests a source area composed of volcanic rocks, coupled with sedimentary sequences rich in wackes, mudstones, and lepto-metamorphosed rocks (Fig. 10). This lithological assemblage resembles the accretionary complex developed in Chile, which includes marine sandstone and mudstone successions associated with a Devonian - early Carboniferous volcanic arc (Hervé et al., 2013, 2016).

## 9. Geochemistry

The whole-rock geochemical analysis of major, trace, and rare earth elements (REE) was performed in fifteen medium-to coarse-grained sandstone samples of the Tepuel Group (Table 5). The geochemical studies of sandstones can be used not only for identifying provenance areas but also to estimate weathering, recycling and diagenetic

**Table 4**
Recalculated modes (normalized to 100%) and petrofacies for the sandstones of the Tepuel Group.

| SAMPLE | Lmm-h+(Lm + Lp)+Qpm | Lv + Lsw + Qmi | Qm + Lss | PETROFACIES |
|---|---|---|---|---|
| Río Genoa Formation | | | | |
| M130 | 75.89 | 1.18 | 22.93 | Quartzose-lithic petrofacies |
| M132 | 31.07 | 0 | 68.93 | Quartzose-lithic petrofacies |
| M132B | 28.75 | 0 | 71.25 | Quartzose-lithic petrofacies |
| M134 | 18.99 | 0 | 81.01 | Quartzose petrofacies |
| M136 | 31.34 | 0 | 68.66 | Quartzose-lithic petrofacies |
| M137 | 20.73 | 0 | 79.27 | Quartzose petrofacies |
| M139 | 15.95 | 0 | 84.05 | Quartzose petrofacies |
| M141 | 28.77 | 0 | 71.23 | Quartzose-lithic petrofacies |
| M143 | 15.66 | 1.21 | 83.13 | Quartzose petrofacies |
| M145 | 32.62 | 2.17 | 65.21 | Quartzose-lithic petrofacies |
| M147 | 21.18 | 0 | 78.82 | Quartzose petrofacies |
| M148 | 39.32 | 1.72 | 58.96 | Quartzose-lithic petrofacies |
| M149 | 27.78 | 0.92 | 71.3 | Quartzose-lithic petrofacies |
| M151 | 24.99 | 0 | 75.01 | Quartzose-lithic petrofacies* |
| M152 | 2.95 | 0.66 | 96.39 | Quartzose petrofacies |
| M153 | 33.03 | 0 | 66.97 | Quartzose-lithic petrofacies |
| M155 | 50.89 | 0 | 49.11 | Quartzose-lithic petrofacies |
| M157 | 20.84 | 0 | 79.16 | Quartzose petrofacies |
| M163 | 17.19 | 5.37 | 77.44 | Quartzose petrofacies |
| ***Mojón de Hierro Formation*** | | | | |
| M61 | 8.28 | 5.73 | 85.99 | Quartzose petrofacies |
| M62 | 18.99 | 7.26 | 73.74 | Quartzose petrofacies |
| M63 | 32.64 | 0 | 67.36 | Quartzose-lithic petrofacies |
| M66 | 12.05 | 3.62 | 84.33 | Quartzose petrofacies |
| M68 | 26.09 | 0 | 73.91 | Quartzose-lithic petrofacies* |
| M89 | 28.21 | 0 | 71.79 | Quartzose-lithic petrofacies* |
| M90 | 21.65 | 30.93 | 47.42 | Volcanic-sedimentary petrofacies |
| M93 | 26.46 | 0 | 73.54 | Quartzose-lithic petrofacies* |
| M94 | 42.11 | 0 | 57.89 | Quartzose-lithic petrofacies |
| M95 | 7.29 | 3.63 | 89.08 | Quartzose petrofacies |
| M99 | 10.52 | 0 | 89.48 | Quartzose petrofacies |
| M104 | 13.89 | 0 | 86.11 | Quartzose petrofacies |
| M108 | 14.43 | 0 | 85.57 | Quartzose petrofacies |
| M111 | 4.37 | 5.84 | 89.79 | Quartzose petrofacies |
| M112 | 16.04 | 0.94 | 83.02 | Quartzose petrofacies |
| M122 | 2.99 | 0 | 97.01 | Quartzose petrofacies |
| M126 | 54.84 | 0 | 45.16 | Quartzose-lithic petrofacies |
| M129 | 11.95 | 1.09 | 86.96 | Quartzose petrofacies |
| ***Pampa de Tepuel Formation*** | | | | |
| M1 | 32.96 | 22.73 | 44.31 | Quartzose-lithic petrofacies |
| M3 | 17.39 | 0 | 82.61 | Quartzose petrofacies |
| M5 | 0 | 0 | 100 | Quartzose petrofacies |
| M14 | 17.38 | 0 | 82.62 | Quartzose petrofacies |
| M17 | 6.72 | 19.32 | 73.96 | Quartzose petrofacies |
| M20 | 0 | 5.89 | 94.11 | Quartzose petrofacies |
| M25 | 3.16 | 5.26 | 91.58 | Quartzose petrofacies |
| M28 | 38.89 | 0 | 61.11 | Quartzose-lithic petrofacies |
| M37 | 25 | 0 | 75 | Quartzose-lithic petrofacies* |
| M41 | 14.93 | 8.96 | 76.11 | Quartzose petrofacies |
| M45 | 27.69 | 0 | 72.31 | Quartzose petrofacies |
| M50 | 15.28 | 1.39 | 83.33 | Quartzose petrofacies |
| M54 | 2.43 | 7.32 | 90.24 | Quartzose petrofacies |
| M55 | 3.91 | 3.91 | 92.17 | Quartzose petrofacies |
| M56 | 6.5 | 6.5 | 87 | Quartzose petrofacies |
| M69 | 0.8 | 2.4 | 96.8 | Quartzose petrofacies |
| M71 | 9.19 | 0 | 90.81 | Quartzose petrofacies |
| M77 | 15.74 | 4.63 | 79.63 | Quartzose petrofacies |
| M83 | 5.69 | 0 | 94.31 | Quartzose petrofacies |
| M84 | 7.53 | 0 | 92.47 | Quartzose petrofacies |
| M87 | 14.48 | 0 | 85.52 | Quartzose petrofacies |
| ***Valle Chico Formation*** | | | | |
| VC1 | 0 | 59.6 | 40.4 | Volcanic-sedimentary petrofacies |
| VC2 | 2.53 | 62.34 | 35.13 | Volcanic-sedimentary petrofacies |
| VC3 | 0 | 66.67 | 33.33 | Volcanic-sedimentary petrofacies |
| VC4 | 1 | 84.46 | 14.54 | Volcanic-sedimentary petrofacies |
| VC4b | 1.04 | 61.31 | 37.66 | Volcanic-sedimentary petrofacies |
| VC5 | 0 | 75.07 | 24.93 | Volcanic-sedimentary petrofacies |
| VC6 | 1.05 | 47.35 | 51.6 | Volcanic-sedimentary petrofacies |
| VC7 | 1.8 | 67.8 | 30.4 | Volcanic-sedimentary petrofacies |
| VC8 | 2.97 | 43.27 | 53.76 | Volcanic-sedimentary petrofacies |
| VC9 | 1.06 | 44.46 | 54.47 | Volcanic-sedimentary petrofacies |
| VC10 | 6.25 | 53.91 | 39.84 | Volcanic-sedimentary petrofacies |
| VC11 | 0 | 32.35 | 67.65 | Volcanic-sedimentary petrofacies |
| VC12 | 0 | 51.56 | 48.44 | Volcanic-sedimentary petrofacies |
| VC13 | 2.35 | 47.07 | 50.58 | Volcanic-sedimentary petrofacies |
| VC14 | 0 | 57.91 | 42.09 | Volcanic-sedimentary petrofacies |
| VC15 | 0 | 51.18 | 48.82 | Volcanic-sedimentary petrofacies |
| VC16 | 0 | 66.95 | 33.05 | Volcanic-sedimentary petrofacies |

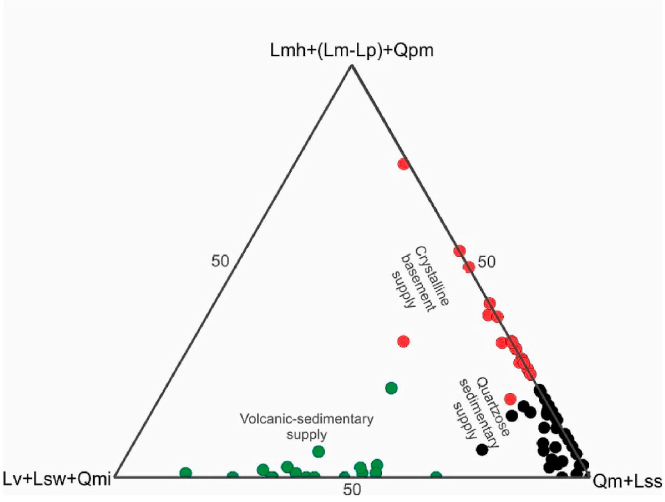


**Fig. 11.** Ternary diagram using key modal components defining petrofacies.

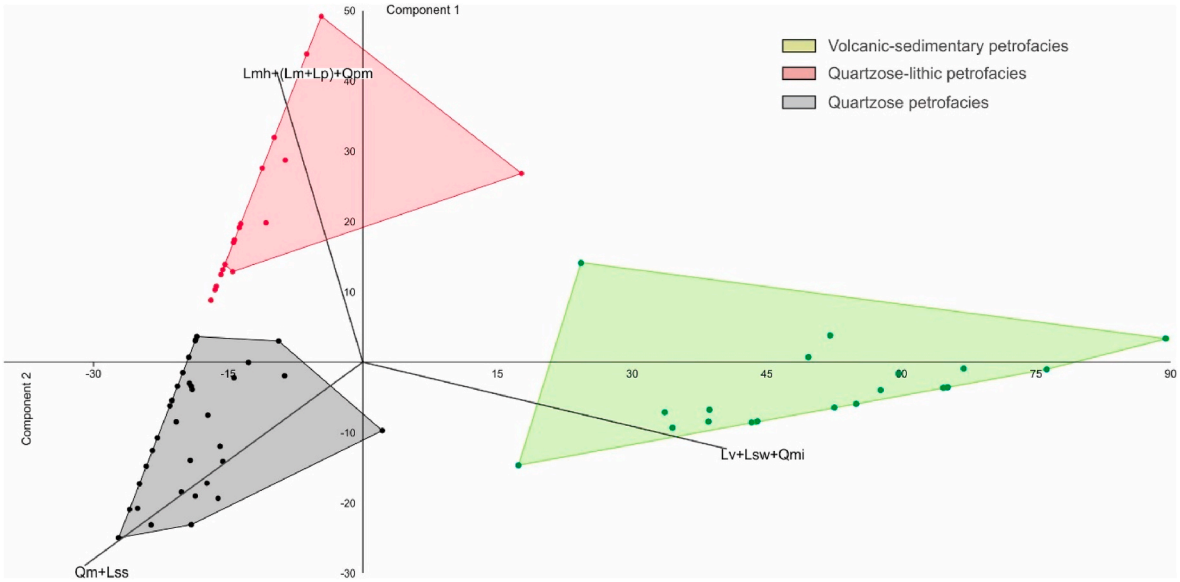


**Fig. 12.** Principal component analysis (PCA) using the key modal components.

processes in sedimentary rocks (Nesbitt and Young, 1984; Roser and Korsch, 1988; Roser et al., 2002; Garzanti and Resentini, 2016; Limarino and Giordano, 2016; Chen and Robertson, 2020).

The sandstones of the Tepuel Group were classified following the geochemical proposals by Pettijohn et al. (1972) and Herron (1988); the results match in a broad way with the petrographic observations since both classification lines show the dominance of litharenites, sublitharenites and feldspathic litharenites (Figs. 7 and 13). However, the presence of greywacke or wackes in the geochemical classifications (Fig. 13) is not supported by petrographic observation.

The samples included in the fields of greywacke and wackes in the geochemical classifications belong to the Valle Chico and Río Genoa formations. In the case of the three samples of the Valle Chico Formation, the framework fraction contains a high amount of volcanic lithic fragments, abundant pseudomatrix (altered lithic clasts), grains of wackes, clasts of mudstones and slates and feldspars. All these features produce a decrease in the $SiO_2/Al_2O_3$ ratios and, at the same time, an increase in the $Na_2O/K_2O$ and $Fe_2O_3/K_2O$ ratios, which lead to an erroneous geochemical classification of the sandstones as greywacke or wackes (and even shale, Fig. 13).

In the case of the Río Genoa Formation, the increase in the feldspar content (both orthoclase and plagioclase) and the micaceous minerals contained in the metamorphic clasts, produce a higher $Na_2/K_2O$ and a lower $SiO_2/Al_2O_3$ ratio and consequently result in a displacement towards the greywacke or wacke fields (Fig. 13).

The relation between petrofacies and geochemical data can be evaluated by comparative analyses of $Fe_2O_3$, $K_2O$, and $SiO_2$. Fig. 14a displays the percentages of $K_2O$ against $SiO_2$, showing that the sandstones have moderate-to low-K values. The low-K values correspond to sandstones of the Pampa de Tepuel and Mojón de Hierro formations that record low values in feldspar (mainly included in the quartzose petrofacies). On the contrary, the highest values of $K_2O$ appear in the Río Genoa Formation, which is dominated by the quatzose-lithic petrofacies and show an increase in the K-feldspar and micaceous minerals with respect to that of the quartzose petrofacies.

Another interesting aspect of the petrographic and geochemical results is found by comparing the percentages of $Fe_2O_3$ against $K_2O$ (Fig. 14b). This diagram shows three different situations: 1. low $Fe_2O_3$ and $K_2O$ contents that match with low values of $Al_2O_3/SiO_2$ in the Pampa de Tepuel and Mojón de Hierro formations, 2. High $Fe_2O_3$ values that coincide with the appearance of abundant pseudomatrix and mudstone grains of the Valle Chico Formation, and 3. high $K_2O$ values, coupled with a decrease in the amount of $Fe_2O_3$, resulting from increasing potassium feldspar abundance in the Río Genoa Formation.

Very long transport distance, enough to eliminate unstable clasts, is a severe limitation for provenance studies using detrital modes of sandstones. In these cases, long transport can delete the provenance signal and hamper the identification of sediment source areas. One way to evaluate this possibility is to use the relationship between Th/Sc versus Zr/Sc, which has been used successfully in previous studies (McLennan, 1989; McLennan et al., 1993; Spalletti et al., 2014; Chen and Robertson, 2019, 2020). A sharp increase in Th/Sc versus Zr/Sc ratios could indicate the recycling of sediments and concentration of ultra-stable minerals (i.e., zircon) during multiple cycles of transport and deposition. However, as pointed out by McLennan et al. (1993), the increase in Zr/Sc and Th/Sc ratios does not necessarily indicate the detrital derivation from recycled sandstones since only petrographic evidence can confirm this assumption. In the case of the Tepuel Group, the Zr/Sc against Th/Sc diagram indicates an affinity with the composition of the upper continental crust and does not suggest a high degree of reworking and concentration of super-stable minerals (Fig. 15a).

Similarly, the ternary diagram Th-Hf-Co is useful in evaluating the concentration of zircon due to sedimentary reworking (Fig. 15b); in these cases, the concentration of zircon grains due to reworking produces a Hf-enrichment and an associated depletion in Co (Basu et al., 1990). Although the Tepuel Group sandstones show some dispersion, almost all the samples are placed near the average values for continental crust, and only one (Pampa de Tepuel Formation) shows certain Hf-enrichment evidencing the increase in the maturity of the grains in quartzose petrofacies.

In short, neither the binary diagram Zr/Sc versus Th/Sc nor the ternary diagram Th-Hf-Co indicate a high concentration of ultra-stable minerals due to sedimentary reworking. That is consistent with the detrital modes obtained from the petrographic studies.

The nature of the provenance areas can be discriminated using the diagram proposed by Roser and Korsch (1988). In this scheme all the samples from to the Sierra de Tepuel area (Pampa de Tepuel and Mojón de Hierro formations) occur in the quartzose field, suggesting derivation of sand from sedimentary terrains (Fig. 16). Petrographic examinations of the sandstones match with this geochemical interpretation since both the Pampa de Tepuel and Mojón de Hierro formations are included in the quartzose and quartzose-lithic petrofacies that show more than 89% and 69% of quartz grains (Fig. 16). For samples with highly negative F1 and F2 factors, Roser and Korsch (1988) defined the P1EXT field as a

**Table 5**
Whole-rock geochemical (major, trace, and RRE) data of Tepuel group sandstones.

| | | | | Río Genoa Fm (n = 3) | | | Mojón de Hierro Fm (n = 2) | | Pampa de tepuel Fm (n = 4) | | | | Valle Chico Fm (n = 6) | | | | | |
|---|---|---|---|---|---|---|---|---|---|---|---|---|---|---|---|---|---|---|
| Analyte and unit Symbol | | Detection Limit | Anal Met | M136 | M145 | M151 | M63 | M104 | M17 | M55 | M50 | M77 | VC1 | VC8 | VC9 | VC11 | VC12 | VC16 |
| SiO2 | % | 0,01 | 1 | 71.31 | 75.46 | 73.51 | 92.96 | 96.38 | 80.33 | 87.6 | 89.27 | 87.69 | 78.32 | 79.53 | 75.99 | 67.97 | 66.96 | 75.7 |
| Al2O3 | % | 0,01 | 1 | 13.35 | 12.57 | 13.67 | 3.67 | 2.07 | 9.28 | 6.07 | 5.22 | 6.38 | 9.68 | 9.26 | 10.94 | 13.56 | 14.3 | 11.78 |
| Fe2O3(T) | % | 0,01 | 1 | 3.78 | 3.21 | 2.73 | 1.01 | 1.18 | 3.42 | 2.2 | 2.25 | 2.24 | 3.92 | 3.8 | 4.21 | 5.95 | 6.17 | 4.1 |
| MnO | % | 0,001 | 1 | 0.05 | 0.035 | 0.032 | 0.009 | 0.013 | 0.038 | 0.022 | 0.022 | 0.018 | 0.055 | 0.075 | 0.051 | 0.092 | 0.092 | 0.047 |
| MgO | % | 0,01 | 1 | 1.42 | 1.03 | 0.79 | 0.2 | 0.06 | 0.84 | 0.19 | 0.41 | 0.42 | 1.03 | 1.01 | 1.28 | 2.23 | 2.56 | 0.9 |
| CaO | % | 0,01 | 1 | 1.04 | 0.47 | 0.22 | 0.25 | 0.03 | 0.21 | 0.06 | 0.11 | 0.08 | 0.81 | 1.51 | 0.98 | 1.65 | 1.44 | 1.13 |
| Na2O | % | 0,01 | 1 | 3.6 | 1.83 | 4.02 | 0.06 | 0.04 | 2.19 | 1.22 | 1.27 | 0.98 | 1.56 | 1.99 | 1.83 | 3.35 | 3.73 | 2.35 |
| K2O | % | 0,01 | 1 | 2.46 | 2.68 | 3 | 0.68 | 0.47 | 1.49 | 1.12 | 0.8 | 1.02 | 2.17 | 1.42 | 2.18 | 2.15 | 1.93 | 2.58 |
| TiO2 | % | 0,001 | 1 | 0.405 | 0.376 | 0.376 | 0.11 | 0.158 | 0.513 | 0.246 | 0.218 | 0.251 | 0.374 | 0.495 | 0.612 | 0.643 | 0.644 | 0.444 |
| P2O5 | % | 0,01 | 1 | 0.07 | 0.08 | 0.1 | 0.01 | <0.01 | 0.09 | 0.05 | 0.05 | 0.09 | 0.07 | 0.11 | 0.12 | 0.12 | 0.1 | 0.06 |
| LOI | % | | 1 | 2.9 | 2.5 | 1.5 | 1.29 | 0.34 | 1.83 | 1.26 | 0.95 | 1.57 | 1.54 | 1.29 | 2.08 | 2.14 | 2.37 | 1.44 |
| Total | % | 0,01 | 1 | 100.4 | 100.2 | 99.94 | 100.3 | 100.7 | 100.2 | 100 | 100.6 | 100.7 | 99.53 | 100.5 | 100.3 | 99.86 | 100.3 | 100.5 |
| Sc | ppm | 1 | 1 | 9 | 8 | 7 | 3 | 1 | 7 | 5 | 4 | 5 | 7 | 9 | 10 | 15 | 16 | 9 |
| Be | ppm | 1 | 1 | 2 | 2 | 2 | <1 | <1 | 1 | <1 | <1 | <1 | 1 | 2 | 2 | 2 | 2 | 2 |
| V | ppm | 5 | 1 | 59 | 58 | 49 | 16 | 9 | 57 | 28 | 26 | 38 | 50 | 61 | 75 | 109 | 117 | 51 |
| Ba | ppm | 2 | 1 | 481 | 341 | 479 | 115 | 45 | 291 | 198 | 159 | 156 | 623 | 403 | 341 | 563 | 587 | 453 |
| Sr | ppm | 2 | 1 | 139 | 56 | 116 | 8 | 12 | 75 | 33 | 28 | 27 | 135 | 182 | 97 | 239 | 262 | 172 |
| Y | ppm | 1 | 1 | 17 | 19 | 14 | 4 | 4 | 18 | 11 | 12 | 10 | 16 | 25 | 24 | 19 | 22 | 26 |
| Zr | ppm | 2 | 1 | 90 | 98 | 94 | 49 | 150 | 134 | 123 | 114 | 76 | 192 | 243 | 221 | 180 | 193 | 180 |
| Cr | ppm | 20 | 2 | 20 | 40 | 20 | <_20 | <_20 | 40 | 20 | 20 | 30 | 40 | 60 | 50 | 80 | 70 | 30 |
| Co | ppm | 1 | 2 | 5 | 28 | 5 | 1 | 1 | 6 | 3 | 2 | 4 | 5 | 8 | 9 | 11 | 13 | 6 |
| Ni | ppm | 20 | 2 | <20 | 30 | <20 | <20 | <20 | 20 | <20 | <20 | <20 | <20 | 20 | 30 | 60 | 20 | <20 |
| Cu | ppm | 10 | 2 | <10 | 10 | <10 | <10 | <10 | 10 | <10 | 10 | <10 | 10 | 20 | 20 | 20 | 20 | 20 |
| Zn | ppm | 30 | 2 | 60 | 60 | 50 | <30 | <30 | 40 | 120 | 30 | 30 | 40 | 90 | 70 | 70 | 90 | 50 |
| Ga | ppm | 1 | 2 | 13 | 14 | 14 | 3 | 2 | 9 | 6 | 5 | 6 | 9 | 9 | 12 | 16 | 16 | 13 |
| Ge | ppm | 1 | 2 | 1 | 1 | 1 | 1 | 1 | 1 | 1 | <1 | 1 | 1 | 1 | 2 | 1 | 2 | 1 |
| As | ppm | 5 | 2 | 6 | 5 | 6 | <5 | <5 | 7 | <5 | 11 | 7 | <5 | 12 | 17 | 9 | 11 | 10 |
| Rb | ppm | 2 | 2 | 89 | 106 | 100 | 25 | 15 | 53 | 40 | 30 | 36 | 75 | 47 | 86 | 74 | 66 | 102 |
| Nb | ppm | 1 | 2 | 6 | 5 | 6 | 1 | 2 | 5 | 3 | 3 | 3 | 5 | 7 | 8 | 8 | 10 | 8 |
| Mo | ppm | 2 | 2 | <2 | <2 | <2 | <2 | 2 | <2 | <2 | 2 | <2 | <2 | <2 | <2 | <2 | <2 | <2 |
| Ag | ppm | 0,5 | 2 | 0.5 | 0.5 | 0.5 | <0.5 | 0.7 | 0.7 | 0.6 | 0.6 | <0.5 | 1.2 | 0.9 | 1.3 | 1.1 | 0.7 | 1.1 |
| In | ppm | 0,2 | 2 | <_0.2 | <_0.2 | <0.2 | <0.2 | <0.2 | <0.2 | <0.3 | <0.2 | <0.2 | <0.2 | <0.2 | <0.2 | <0.2 | <0.2 | <0.2 |
| Sn | ppm | 1 | 2 | 2 | 2 | 3 | 1 | 1 | 2 | 1 | 1 | 1 | 2 | 3 | 3 | 3 | 2 | 4 |
| Sb | ppm | 0,5 | 2 | 0.6 | 0.5 | <0.5 | <0.5 | <0.5 | 0.7 | <0.5 | 0.6 | <0.5 | <0.5 | 0.8 | <0.5 | 1 | 2.3 | 0.6 |
| Cs | ppm | 0,5 | 2 | 2.8 | 3.7 | 2.5 | 0.7 | 0.6 | 1.9 | 1.1 | 0.8 | 2.2 | 1.8 | 1.3 | 4.7 | 2.2 | 1.9 | 4.2 |
| La | ppm | 0,1 | 2 | 25.1 | 29.6 | 20.9 | 5.4 | 5.2 | 20.2 | 12.2 | 13.4 | 10.3 | 23.1 | 31.5 | 32.1 | 29 | 28.4 | 28.9 |
| Ce | ppm | 0,1 | 2 | 47.7 | 56.6 | 40.3 | 10.5 | 9.4 | 38.5 | 23.6 | 25.9 | 19 | 46 | 64.4 | 63.4 | 57.7 | 59.7 | 57.8 |
| Pr | ppm | 0,05 | 2 | 5.41 | 6.88 | 4.86 | 1.25 | 1.11 | 4.86 | 2.77 | 3.08 | 2.3 | 5.46 | 7.03 | 7.56 | 6.82 | 6.61 | 7.14 |
| Nd | ppm | 0,1 | 2 | 19.8 | 25.4 | 17.7 | 4.6 | 3.8 | 18.1 | 10.3 | 11.5 | 8.8 | 20.1 | 26.4 | 28.6 | 25.7 | 26.4 | 26.3 |
| Sm | ppm | 0,1 | 2 | 3.8 | 5.1 | 3.5 | 0.9 | 0.7 | 3.9 | 2 | 2.3 | 1.8 | 3.9 | 5.7 | 5.6 | 5.1 | 5.1 | 5.4 |
| Eu | ppm | 0,05 | 2 | 0.92 | 1.09 | 0.93 | 0.19 | 0.15 | 0.84 | 0.43 | 0.53 | 0.36 | 0.76 | 1.07 | 1.03 | 1.18 | 1.27 | 0.89 |
| Gd | ppm | 0,1 | 2 | 3.3 | 3.9 | 2.9 | 0.7 | 0.6 | 3.3 | 1.9 | 2.1 | 1.7 | 3.4 | 5.2 | 5 | 4.4 | 4.6 | 4.8 |
| Tb | ppm | 0,1 | 2 | 0.6 | 0.6 | 0.4 | 0.1 | <_0.1 | 0.5 | 0.3 | 0.3 | 0.3 | 0.5 | 0.8 | 0.8 | 0.7 | 0.7 | 0.8 |
| Dy | ppm | 0,1 | 2 | 3.3 | 3.5 | 2.7 | 0.7 | 0.6 | 3.2 | 2 | 2.1 | 1.8 | 3.1 | 4.5 | 4.7 | 4.1 | 4.1 | 4.6 |
| Ho | ppm | 0,1 | 2 | 0.6 | 0.7 | 0.5 | 0.1 | 0.1 | 0.6 | 0.4 | 0.4 | 0.4 | 0.6 | 0.9 | 0.9 | 0.8 | 0.8 | 0.9 |
| Er | ppm | 0,1 | 2 | 1.9 | 1.9 | 1.5 | 0.4 | 0.4 | 1.9 | 1.3 | 1.3 | 1.1 | 1.7 | 2.7 | 2.7 | 2.3 | 2.4 | 2.8 |
| Tm | ppm | 0,05 | 2 | 0.29 | 0.28 | 0.22 | 0.06 | 0.06 | 0.27 | 0.19 | 0.2 | 0.16 | 0.26 | 0.38 | 0.42 | 0.34 | 0.37 | 0.41 |
| Yb | ppm | 0,1 | 2 | 1.9 | 1.9 | 1.5 | 0.4 | 0.4 | 1.8 | 1.3 | 1.4 | 1.1 | 1.8 | 2.5 | 2.8 | 2.3 | 2.5 | 2.9 |
| Lu | ppm | 0,01 | 2 | 0.29 | 0.29 | 0.23 | 0.08 | 0.07 | 0.27 | 0.2 | 0.22 | 0.18 | 0.28 | 0.39 | 0.44 | 0.35 | 0.36 | 0.46 |
| Hf | ppm | 0,2 | 2 | 2.6 | 2.3 | 2.5 | 1.2 | 3.3 | 3.5 | 3.1 | 2.8 | 2.1 | 5.1 | 5.5 | 5.7 | 4.8 | 4.3 | 4.9 |
| Ta | ppm | 0,1 | 2 | 0.6 | 0.6 | 0.6 | 0.1 | 0.2 | 0.5 | 0.3 | 0.3 | 0.3 | 0.5 | 0.6 | 0.8 | 0.8 | 0.8 | 0.9 |
| W | ppm | 1 | 2 | <1 | 1 | <1 | <1 | <1 | <1 | 2 | <1 | <1 | <1 | 2 | 1 | 2 | 3 | 2 |
| Tl | ppm | 0,1 | 2 | 0.5 | 0.6 | 0.6 | 0.2 | 0.1 | 0.3 | 0.2 | 0.2 | 0.2 | 0.4 | 0.3 | 0.5 | 0.4 | 0.4 | 0.7 |
| Pb | ppm | 5 | 2 | 17 | 18 | 14 | <5 | <5 | 10 | <5 | <5 | 7 | 18 | 23 | 21 | 27 | 50 | 13 |
| Bi | ppm | 0,4 | 2 | <0.4 | <0.4 | <0.4 | <0.4 | <0.4 | <0.4 | <0.4 | <0.4 | <0.4 | <0.4 | <0.4 | <0.4 | 0.5 | 0.4 | <0.4 |
| Th | ppm | 0,1 | 2 | 7.3 | 7.6 | 6.7 | 1.8 | 1.6 | 4.8 | 3.8 | 3.3 | 3.3 | 7.4 | 9.2 | 10.2 | 9.1 | 8.6 | 12.5 |
| U | ppm | 0,1 | 2 | 1.9 | 2.2 | 1.3 | 0.6 | 0.5 | 1.3 | 1.7 | 0.9 | 0.9 | 2 | 2.1 | 2.6 | 2.2 | 2.1 | 3 |

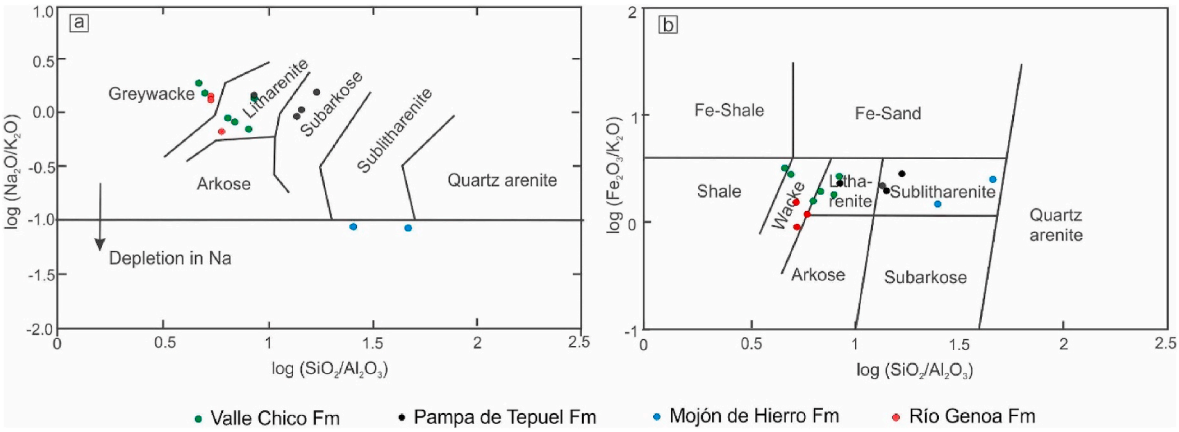


**Fig. 13.** Geochemical classifications of the Tepuel Group sandstones: a. $Na_2O/K_2O$ versus $SiO_2/Al_2O_3$ discrimination diagram (after Pettijohn et al., 1972) and b. $Fe_2O_3/K_2O$ versus $SiO_2/Al_2O_3$ diagram (after Herron, 1988).

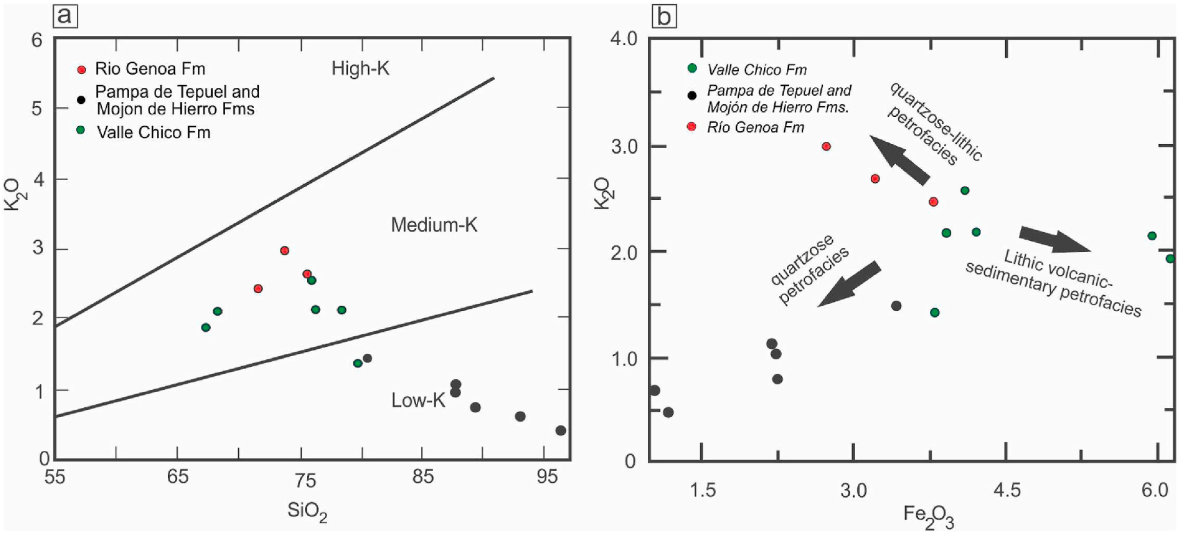


**Fig. 14.** a. $K_2O$ vs $SiO_2$ and b. $Fe_2O_3$ vs $K_2O$ diagrams.

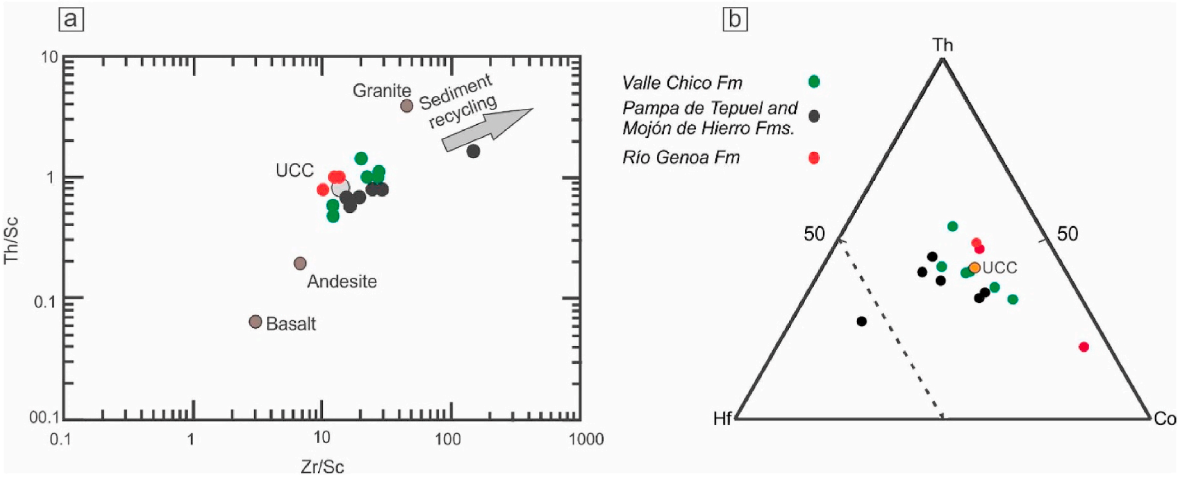


**Fig. 15.** a. Zr/Sc vs Th/Sc diagram and b. ThHfCo ternary diagram.

derivation of volcanic rocks of different nature. All the sandstones of the Valle Chico Formation are included in the P1EXT, reflecting the volcanic supply coupled with sedimentary and metamorphic clasts recorded in the thin sections (Tables 2 and 3 and Fig. 16). The interpretation of the three samples belonging to the Río Genoa Formation is complex, since they plot into the P1EXT field, although the proportion of volcanic clasts

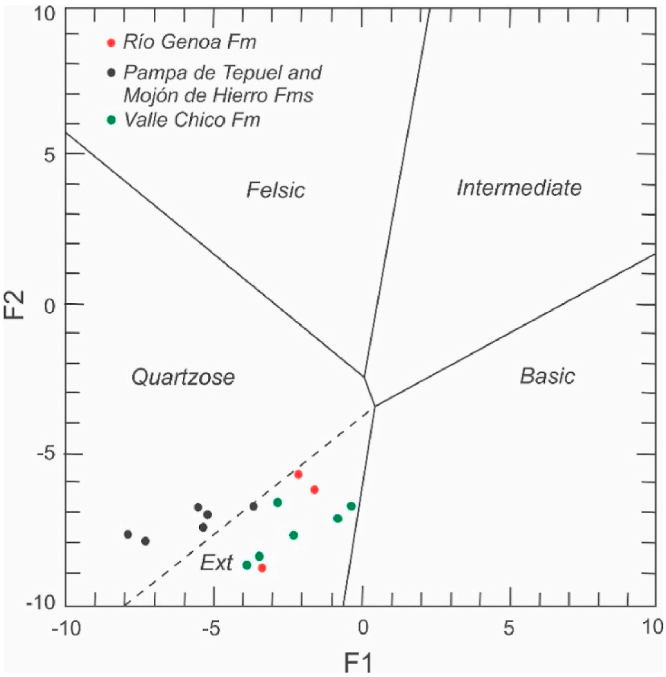


**Fig. 16.** Roser and Korsch (1988) diagram of the Tepuel group samples. The discriminant functions are: F1= (−1.773*$TiO_2$) + (0.607*$Al_2O_3$) + (0.760*$Fe_{2O3}$) + (−1.500*MgO) + (0.616*CaO) + (0.509*$Na_2O$) + (−1.224*$K_2O$) + (−9.090); F2 = (0.445*$TiO_2$) + (0.070* $Al_2O_3$) + (−0.250* $Fe_2O_3$) + (−1.142*MgO) + (0.438*CaO) + (1.475*$Na_2O$) + (−1.426*$K_2O$) + (−6.861).

is very low. This situation probably reflects the transition between the quartzose sedimentary field (Pampa de Tepuel and Mojón de Hierro formations) and the volcanic-sedimentary supply of the Valle Chico Formation. Another possibility is the Roser and Korsch (1988) diagram shows some uncertainty to discriminate provenance areas for very negative values of F1 and F2.

Another way to analyze the Roser and Korsch (1988) model is by using the relationship between the percentages of $SiO_2$ and $Al_2O_3$ (Fig. 17). The higher percentages of $SiO_2$ content observed in the Pampa de Tepuel and Mojón de Hierro formations, when compared with Río Genoa and Valle Chico formations (Fig. 17), fall within the quartzose

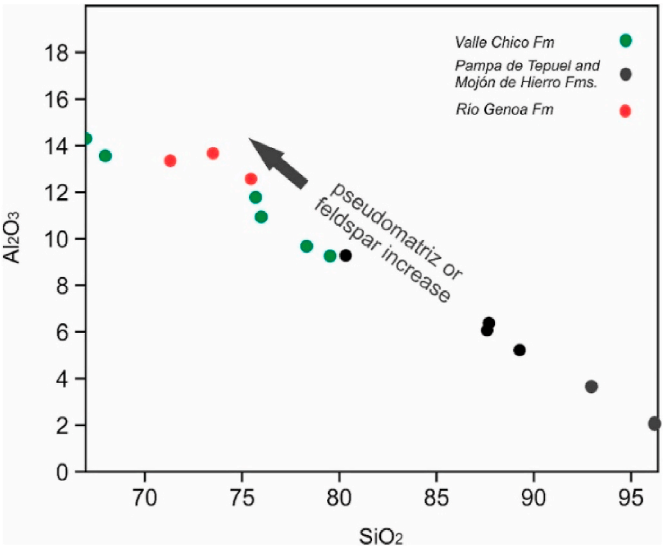


**Fig. 17.** $SiO_2$ vs $Al_2O_3$ diagram.

field of these sandstones in the diagram by Roser and Korsch (1988). Moreover, the correlation between $SiO_2$ and $Al_2O_3$ does not suggest significant compositional discontinuities in the sandstones. On the other hand, the progressive increase in $Al_2O_3$ in the Río Genoa and Valle Chico formations (Fig. 17) reflects not only the increase in the number of feldspar grains (both as monocrystalline grains and forming the groundmass of the volcanic clasts) but also the presence of low- and medium-grade metamorphic rock fragments containing abundant micaceous minerals.

The percentages of trace elements are shown in Table 5, and compared with the average of the upper continental crust show a low concentration of trace elements in all the studied units (between ~1 and 0.1), but exhibiting some differences among the formations (Fig. 18a). Firstly, the sandstones from the Valle Chico Formation show a closer distribution of trace elements to those in the upper continental crust, but the sandstones show slightly positive ratios of lithophile elements such as Th, Zr, Sm, Y, Yb, and Lu. The Pampa de Tepuel and Mojón de Hierro formations show more depleted ratios than those of the Valle Chico Formation, and in the case of Mojón de Hierro sandstones, they display low ratios (lower than 0.5) in Sr and high field strength elements (Ta and Nb, Fig. 18).

The Rare Earth Element (REE) concentrations (Table 5) were normalized to the Upper Continental Crust (UCC) average in Fig. 18b. Similar to trace elements, the REE ratios are closer to the average upper continental crust for sandstones from the Valle Chico and Río Genoa formations, ranging from 1.05 to 1.65. On the contrary, the sandstones of the Mojón de Hierro Formation show REE ratios separated from the rest of the units with depletion values ranging from 0.2 to 0.1.

The distribution of major elements in the studied formations was studied using Principal Component Analysis (Aitchison, 2003; Zhang et al., 2014; Chen and Robertson, 2020). The results show the geochemical differences between the Valle Chico, Río Genoa, Pampa de Tepuel, and Mojón de Hierro formations (Fig. 19). The Valle Chico samples are characterized by high amounts of $Fe_2O_3$, partially MgO and CaO, and discrete proportions of $Ti_2O$ and MnO, while the Río Genoa Formation is defined by the proportions of $Al_2O_3$, $K_2O$, and $Na_2O$. In the case of the units outcropping in the Sierra de Tepuel area, the Pampa de Tepuel and Mojón de Hierro formations, they show similar composition defined by the values of SiO2.

## 10. Discussion

Petrographic and geochemical information improves the knowledge about the provenance areas for the sandstones of the Tepuel Group. In particular, petrographic data allows identification of three petrofacies that correspond to, at least, three main supply areas. The quartzose-lithic petrofacies represents the contribution of crystalline rocks, which, according to a regional framework, likely correspond to sources from the Deseado Massif basement (Fig. 20).

The sandstones belonging to the quartzose petrofacies most likely were derived from the erosion of sedimentary terrains, which explains the relatively high amount of monocrystalline quartz grains and the lower percentages of lithic fragments. The composition of the scarce sandstone lithic grains suggests that provenance areas included mature sandstones rather than immature matrix-rich sandstones. An important issue is the compositional relation between quartzose and quartzose-lithic petrofacies. The ternary diagram of Fig. 11 shows a continuous trend in the composition of the samples along the axis Lmh+(Lm-Lp)+ Qpg – Qm + Lss suggesting that the crystalline basement, and its sedimentary cover, could have supplied sediments simultaneously, although in different proportions (Fig. 11). If this interpretation is correct, both petrofacies formed a unique petrosome, the term used by identifying the consanguineous contribution of a supply area that includes two or more petrofacies (Ingersoll and Cavazza, 1991; Net and Limarino, 2006).

The volcanic-sedimentary petrofacies is here interpreted as the provenance of volcanic rocks coupled with sedimentary terrains.

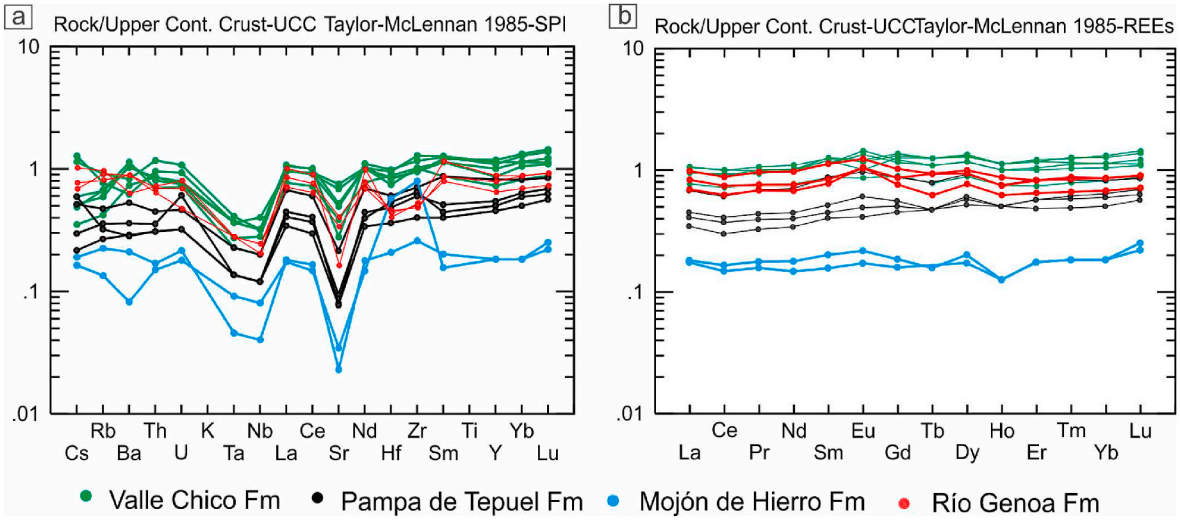


**Fig. 18.** a. Multi-element abundance diagrams and b. REE multi-element abundance diagrams of Tepuel group samples, average Upper Continental Crust (UCC) of Taylor and McLennan (1985).

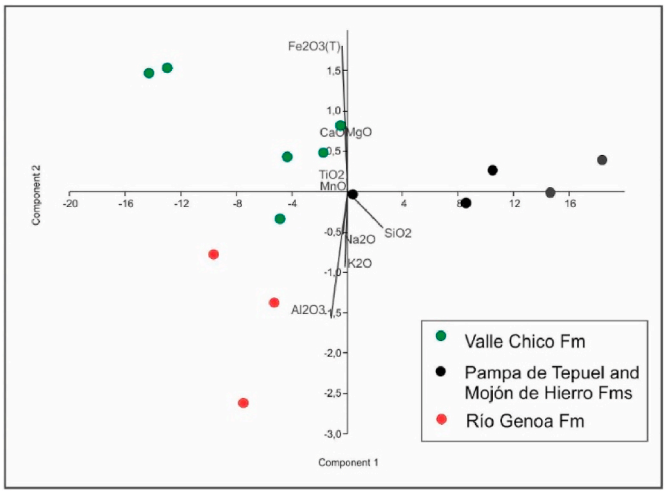


**Fig. 19.** Principal component analysis (PCA) of the major geochemical elements. Note the grouping of samples of each formation.

Different from the quartzose-lithic petrofacies, sedimentary clasts of sandstones in the volcanic-sedimentary petrofacies seem to be wackes and immature sandstones, associated with sandy mudstones and mudstones; these grains were probably the result of low-grade of metamorphism. The volcanic-sedimentary petrofacies allows for two interpretations for source areas as they could have been derived from two different supply areas. The first interpretation assumes that the volcanic-sedimentary petrofacies was supplied by the Devonian-early Carboniferous accretionary complex developed in Chile (Fig. 20). In this scheme, sedimentary clasts would represent the erosion of interbedded sandstone and mudstone successions formed in the Middle Devonian-Carboniferous accretionary prism. At the same time, volcanic clasts would correspond to the Devonian and early Carboniferous volcanic arc that developed mainly in western Chile (Pankhurst et al., 2006; Martínez et al., 2012, Hervé et al., 2013, 2018).

The second possibility for the source of sandstones in the volcanic-sedimentary petrofacies is to suppose that the source area was located to the east of the Tepuel-Genoa Basin, and formed by the erosion of the western volcanic arc considered by Ramos (2008). In this interpretation acidic and mesosilicic clasts would correspond to the volcanic component of the arc association (point 4 in Fig. 2), while mudstones and sandstones would represent a supply of grains from the Cushamen Formation (point 6 in Fig. 2).

Currently, it is not possible to discard either of the two possibilities listed above for the source of the volcanic-sedimentary petrofacies, mainly because this petrofacies was recorded only for sandstones in the Esquel area, and paleocurrent data are ambiguous for establishing a general pattern of circulation during the early Carboniferous. The only evidence for resolving this problem could arise from the analysis of Fig. 11, in which there is no trend in the composition of the samples along the Lmh+(Lm-Lp)+Qpg – Lv + Lsw + Qmi axis. This fact, as opposed to what happens along the Lmh+(Lm-Lp)+Qpg - Qm + Lss axis, would suggest that the supply from the basement (quartzose-lithic petrofacies) and volcanic-sedimentary areas (volcanic-sedimentary petrofacies) were located in different paleogeographic regions from the provenance for sandstones of the volcanic-sedimentary petrofacies.

Although the possibility of the development of a volcanic arc in the central areas of Patagonia cannot be ruled out, the detrital modes indicate provenance from the crystalline basement and sedimentary terrains rather than volcanic arcs during the deposition of the Pampa de Tepuel, Mojón de Hierro and Río Genoa formations (Fig. 20). A different situation occurs in the Valle Chico Formation, where volcanic contributions were recorded during the Early Carboniferous. In this case, it seems more likely that the supply area would correspond to the accretionary prism developed in Chile (Fig. 20).

Beyond the location of the volcanic arc, petrofacies of the Tepuel Group show interesting changes (Fig. 21). The northwesternmost outcrops in the basin, belonging to the Valle Chico Formation (Mississippian), are exclusively formed by the volcanic-sedimentary petrofacies. At the same time, the Pampa de Tepuel Formation (Late Mississippian-early Permian) is made up of quartzose petrofacies and, to a lesser extent, by quartzose-lithic petrofacies (Fig. 21). The quartzose petrofacies also dominates the top of the Sierra de Tepuel section (Mojón de Hierro Formation, early Permian), but shows a considerable increase in the importance of the quartzose-lithic petrofacies contribution through time (Fig. 21). Finally, the Río Genoa Formation (the southernmost in the basin) is dominated by quartzose-lithic petrofacies, together with a low amount of sandstones corresponding to the quartzose petrofacies. According to these data, we can infer that the changes in petrofacies respond to lateral variations in the supply, rather than vertical modifications related to tectonic events.

The geochemical information allows for more precise interpretations about the geotectonic nature of the various provenance areas. The Roser and Korsch (1986) diagram uses the $SiO_2$ against $K_2O/Na_2O$ ratio for

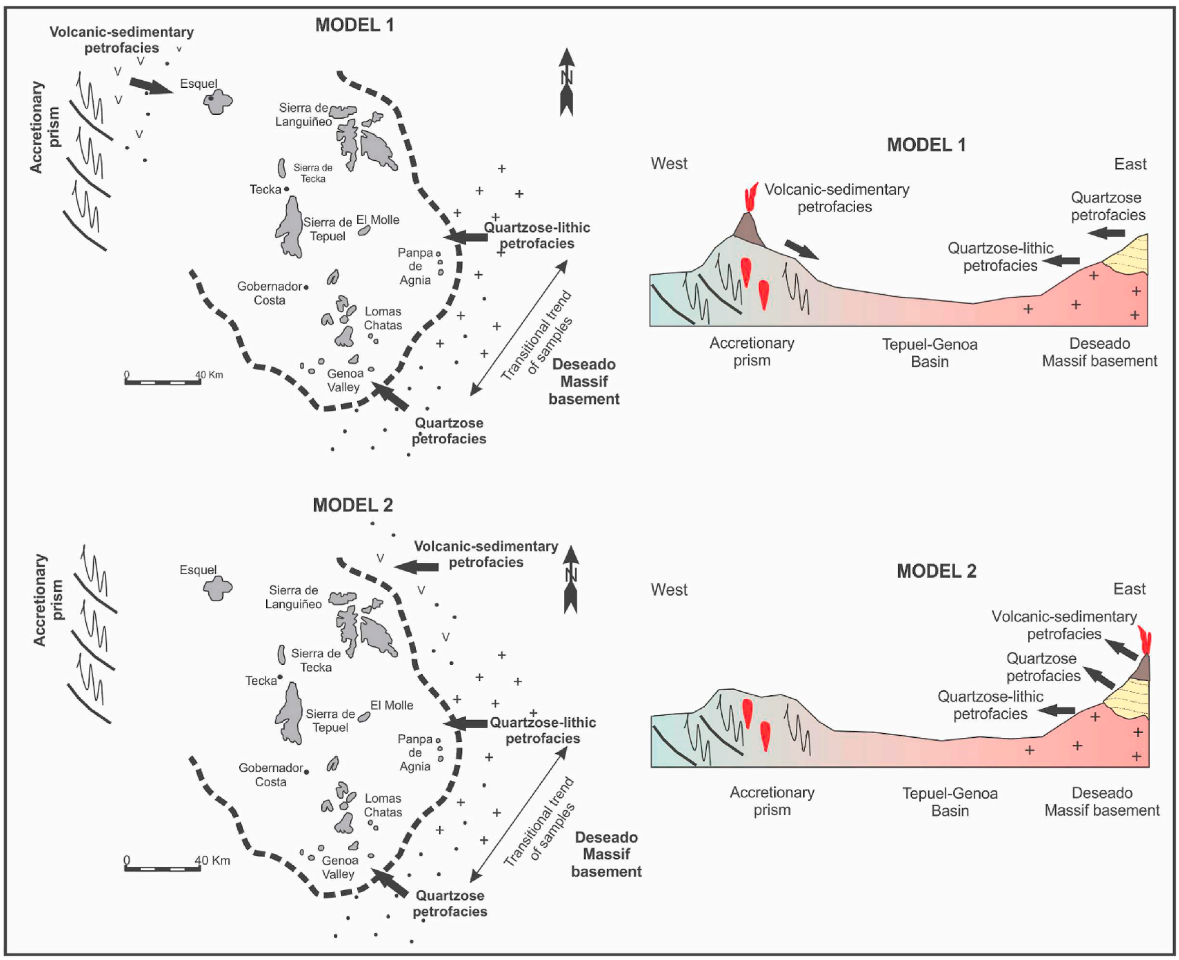


**Fig. 20.** Two different provenance models for the Tepuel-Genoa Basin.

discriminating passive margins, active continental margins, and island arcs. The samples of the Pampa de Tepuel and Mojón de Hierro formations, dominated by the quartzose petrofacies, are included in the passive margin field, while the rest of the samples, belonging to the Valle Chico (volcanic-sedimentary petrofacies), and Río Genoa formations (quartzose-lithic petrofacies) occur in both passive and active continental margin fields (Fig. 22). One of the important limitations of this diagram is the use of major elements since some of them ($K_2O$ and $Na_2O$)

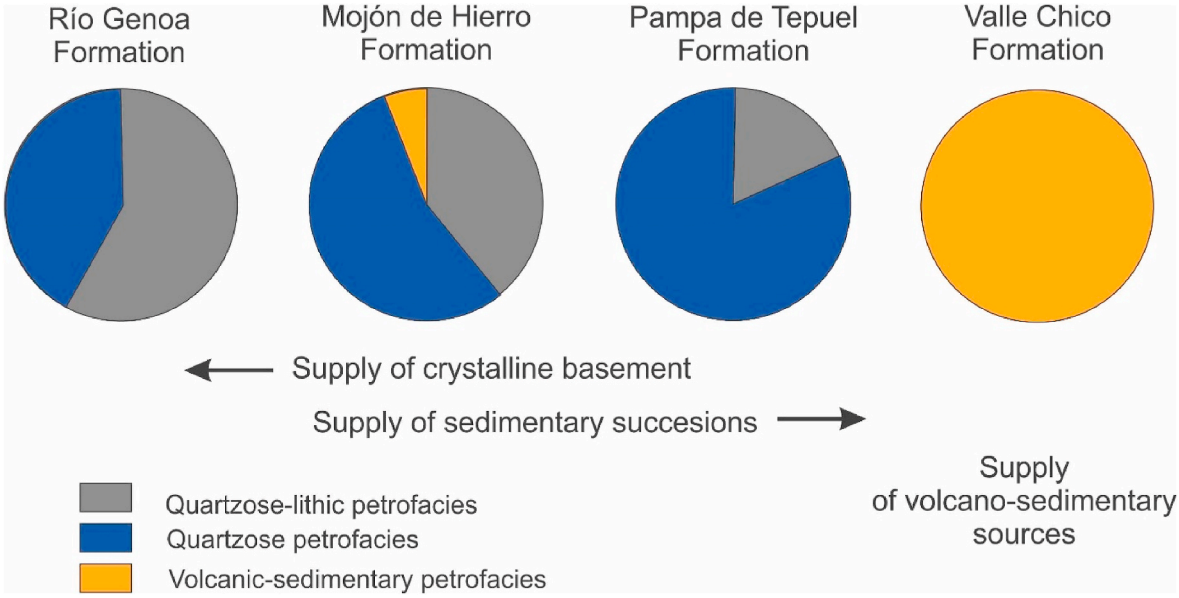


**Fig. 21.** Petrofacies distribution for each formation.

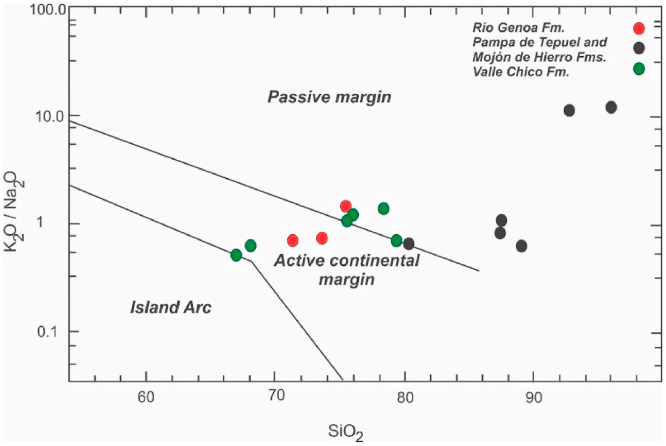


**Fig. 22.** Roser and Korsch (1986) diagram of provenance for the Tepuel Group sandstones.

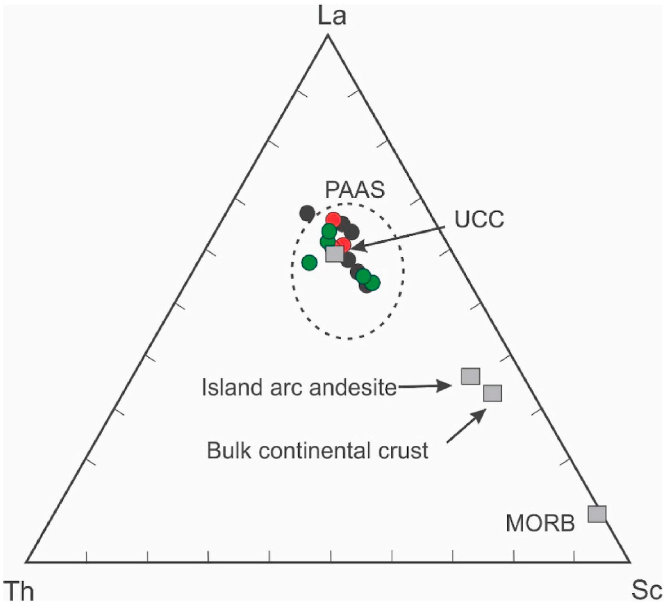


**Fig. 24.** LaThSc ternary diagram of the Tepuel Group sandstones. Note all samples analyzed plotted in the upper continental crust (UCC) near to the Post-Archean Australian Shale (PAAS).

can mobilize during the weathering and diagenesis (Zhang et al., 2014; Chen and Robertson, 2020). Recently, Verma and Armstrong-Altrin (2016), based on a worldwide database of active and passive margin settings, indicated that the Roser and Korsch (1986) and Bhatia (1983) diagrams have limitations for separating active from passive margins.

For better identification of the source areas including characterization of the crust, the percentages of minor and trace key elements such as La, Th, Hf, and Sc can be used (i.e. La/Th vs. Hh, Floyd and Leveridge, 1987). In this diagram, the samples of the Tepuel Group occur near the upper continental crust average but are separated into two groups (Fig. 23a). Samples belonging to the Valle Chico Formation plot in the acidic arc source field, while the samples corresponding to the Pampa de Tepuel, Mojón de Hierro, and Río Genoa formations plot separately due to the lower amount of Hf (Fig. 23b).

Besides the Floyd and Leveridge (1987) diagram, the proportions of La, Th, and Sc were additionally used for characterizing the type of basement exposed in the source areas (Taylor and McLennan, 1985; Jahn and Condie, 1995; Spalletti et al., 2014; Chen and Robertson, 2020). The triangle of Fig. 24 shows that all the Tepuel Group sandstones plot close to the upper continental crust average (UCC), almost entirely in the field of the Post-Archean Australian Shale (PAAS), suggesting a mixed felsic/basic source.

U–Pb ages on detrital zircons from a diamictite sample near the base of the Pampa de Tepuel Formation and a pebbly mudstone sample from near the base of the Mojón de Hierro Formation were obtained by Griffis et al. (2009). The Pampa de Tepuel sample has a dominant age peak of 420 Ma, a much smaller secondary peak at 1040 Ma with lesser peaks at 900, 1180, 2110, and 2630 Ma. The U–Pb 420 Ma peak overlaps with the 425 ± 4 Ma U–Pb zircon ages from the El Sacrifico Granite indicating that the Deseado Massif served as a source area for the Tepuel Basin during deposition of the Pampa de Tepuel Formation (Pankhurst et al., 2003; Griffis et al., 2019).

The Mojón de Hierro Formation sample has a dominant age peak at

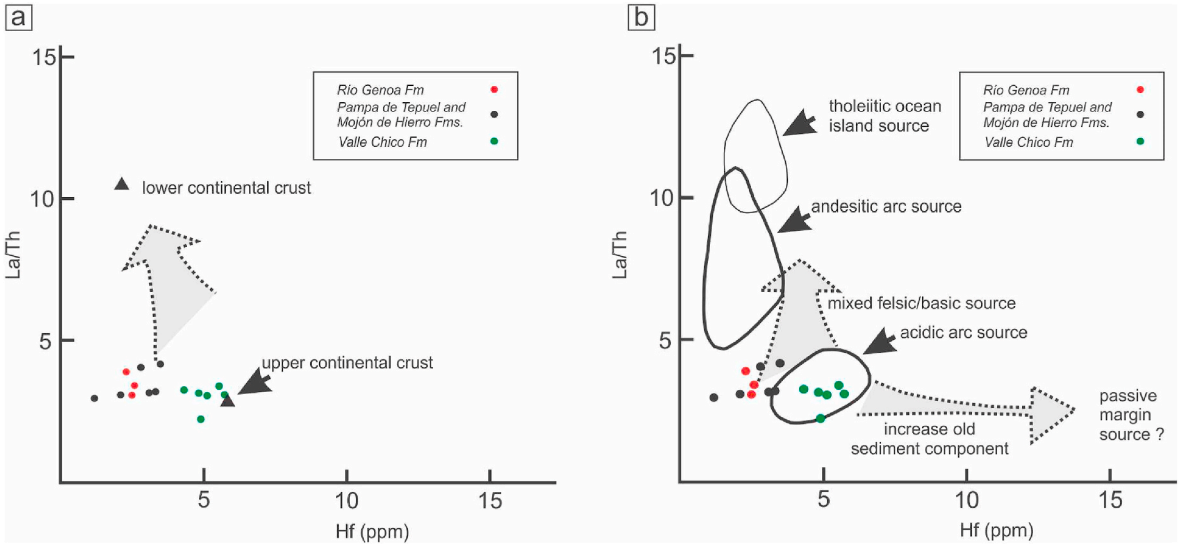


**Fig. 23.** La/Th vs Hh diagrams proposed by Floyd and Leveridge (1987), a. Tepuel Group sandstones plot in upper continental crust and b. The Valle Chico samples indicate an acidic arc source, which differs from the rest of the sandstone samples that indicate a mixed felsic/basic source.

570 Ma, and smaller secondary peaks of 420 and 1060 Ma with minor peaks at 1190 and 2700 Ma (Griffis et al., 2019). The 420 Ma zircons were probably derived from the Deseado Massif. Even though the dominant 570 Ma peak is similar to slightly younger detrital zircon U–Pb peaks in the El Jaguelito and Nahuel Niyeu formations (515–535 Ma) in the North Patagonian Massif, Griffis et al. (2019) negated that region as a source area due to the absence of 420 Ma zircons. Those authors noted an overlap between U–Pb ages and Hf isotope compositions in the detrital zircons of the Mojón de Hierro Formation with zircon populations from widely distributed sites in Antarctica including the Trinity Peninsula Group in the Antarctic Peninsula; the Swanson Formation in Marie Byrd Land; and Cambrian to Carboniferous strata in the Ellsworth Mountains (Flowerdew et al., 2007; Bradshaw et al., 2012; Elliot et al., 2015, 2016; Yakymchuk et al., 2015; Craddock et al., 2019; Griffis et al., 2019); which lead them to suggest that an ice sheet centered in the Ellsworth Mountain block supplied sediment to the Tepuel Basin at that time. However, it should be noted, that McNall (2019) reported that ice sheets were not feeding sediment directly into the Tepuel Basin during deposition of the lower Mojón de Hierro Formation and Pankhurst et al. (2003) identified age peaks (565, 590, 630, 1000 and 1060 Ma, with lesser peaks at 780, 865 and 1180 Ma) in the Dos Hermanos Phyllite of the Deseado Massif. Pankhurst et al. (2003) did not report on detrital zircons Hf isotopic compositions. The overlap of the detrital zircon ages from the Dos Hermanos Phyllite and the zircon ages from the El Sacrifico Granite with detrital zircon age peaks, in both the Pampa de Tepuel and Mojón de Hierro formations, suggest that the Deseado Massif is a more parsimonious source area for the central and southeastern portions of the Tepuel Basin than a more distant Antarctic provenance. During the early Paleozoic to the Carboniferous, several paleogeographic reconstructions place Patagonia adjacent to the Ellsworth Mountain Block in Antarctica (Ramos and Naipauer, 2014; Renda et al., 2019). If those models are correct, then Cambrian to Carboniferous rocks in the Deseado Massif, the Antarctic Peninsula, and the Ellsworth Mountains should display similarities in zircon and detrital zircon age populations.

## 11. Conclusions

1. The sandstones in the Tepuel-Genoa Basin consist mainly of feldspathic litharenites and litharenites, with a minor proportion of lithic feldsarenites and very scarce felsdarenites and sublitharenites. However, there is a sharp difference in the composition of lithic fragments from the northern part of the basin is compared to those in the central and southern areas of the basin. While in the Valle Chico Formation, lithic fragments are dominated by volcanic, immature sandstones and mudstone clasts (probably some lepto-metamorphized), in the Pampa de Tepuel, Mojón de Hierro and Río Genoa formations lithic clasts derived from the crystalline basement prevail.
2. The main types of cement in the Pampa de Tepuel, Mojón de Hierro, and Río Genoa formations are quartz (as quartz overgrowths, megaquartz, and rarely microquartz), rims of chlorite-illite and less frequently occluding kaolinite cement. Calcite occurs as pore-filling intergranular cement, or as patches of calcite seen replacing grains or portions of grains. Traces of feldspar overgrowths were also observed in some feldspathic litharenites and feldsarenites. In the case of the Valle Chico Formation, authigenic minerals consist of rims cement of chlorite, pore-filling microquartz and calcite, quartz overgrowths, and very scarce kaolinite cement. All the studied sandstones show a high degree of mechanical and, in some cases, chemical compaction forming sutured contacts between quartz grains and displacement of twin lamellae in feldspar grains. Deformation of metamorphic grains with ductile behavior produced limited formation of pseudomatrix in some sandstones, but the degree of pseudomatrix increases sharply in the Valle Chico Formation owing to the high amount of volcanic and sedimentary clasts.
3. Seven modal components were recognized that are useful for identifying provenance areas (Qm, Qi, Lv, Lmm-h, Lm-Lp, Lm, Qpm). These components allowed to identify three petrofacies in the sandstones of the Tepuel Group: 1. Quartzose-lithic ($Qm_{69}Lv_2Lm_{29}$), 2. Quartzose ($Qm_{89}Lv_4Lm_7$) and 3. Volcanic-sedimentary ($Qm_{60}Lv_{38}Lm_1$, Fig. 10). The petrofacies division was validated using Principal Component Analysis and triangular diagrams that show no overlapping petrofacies fields.
4. The quartzose-lithic petrofacies is mainly composed of monocrystalline quartz and medium-to high-grade metamorphic clasts, together with scarce mylonites and fine-grained granitoids. This petrofacies is interpreted as derived from crystalline rocks and probably represent sediment supply from the Deseado Massif. The quartzose petrofacies is formed by monocrystalline quartz clasts, with a rare contribution of metamorphic fragments and extremely low percentages of volcanic grains. Contribution from sedimentary terrains, probably covering the crystalline basement of the Deseado Massif, is interpreted as the provenance area. Volcanic-sedimentary petrofacies is made up of acidic and mesosilicic volcanic rock fragments, sedimentary grains (sandstones and mudstones), and idiomorph quartz clasts.
5. The provenance area of the volcanic-sedimentary petrofacies allows for two different interpretations for the location of the source rocks: 1) the volcanic and sedimentary clasts were supplied from the Devonian-early Carboniferous accretionary complex developed in Chile or 2) the clasts came from the western volcanic arc located in the central area of Patagonia to the east of the Tepuel-Genoa Basin. According to the information discussed in this paper, the first possibility seems to be the most likely.
6. Both the binary Th/Sc versus Zr/Sc diagram and the triangular Th-Hf-Co diagram show that the sandstones of the Tepuel Group derived from rocks compatibles with the average composition of the upper continental crust. Moreover, Th/Sc and Zr/Sc ratios and the amount of Hf indicate that the sandstones did not suffer such long transport distance to delete the whole unstable grain populations, which would have masked the characteristics of the provenance areas.
7. The relationships between $SiO_2$ and $K_2O/Na_2O$ (Roser and Korsch, 1986 diagram) suggest that the Pampa de Tepuel and Mojón de Hierro formations represent sedimentation in a passive margin field, while the Valle Chico and Río Genoa formations occur in the fields of the passive and active continental margin. Distributions of minor and REE elements characterized the Valle Chico Formation petrofacies as derived from an acidic arc while the Pampa de Tepuel, Mojón de Hierro, and Río Genoa formations occupied an intermediate position due to low values of Hf.
8. According to the information given by detrital modes and geochemical analysis, the basement of the Macizo del Deseado was the main source in the eastern and central areas of the basin. Low-grade metamorphic, sedimentary, and volcanic rocks, belonging to the accretionary complexes developed in Chile, resulted in the principal source for the western region.

## Authorship contribution statement

**Patricia L. Ciccioli:** Conceptualization, Methodology, Supervision, Writing - original draft. **Carlos O. Limarino:** Conceptualization, Methodology, Supervision, Writing - original draft. **John L. Isbell:** Conceptualization, Methodology, Writing - original draft. **Arturo C. Taboada:** Conceptualization, Methodology. **María A. Pagani:** Conceptualization, logistic fieldwork. **Erik L. Gulbranson:** Conceptualization, Methodology.

## Declaration of competing interest

The authors declare that they have no known competing financial

interests or personal relationships that could have appeared to influence the work reported in this paper.

## Acknowledgments

The authors appreciate the comments and suggestions provided by Maisa Tunik and Luis Spalletti reviewers that let improve the manuscript. This project was supported financially by grants from ANPCyT 2016–1312 to COL, the U.S. National Science Foundation (OISE-1444181, OISE-1559231, and EAR-1729219) and the UW-Milwaukee Research Growth Initiative (RGI) to JLI. The authors thank the support of the Universidad de Buenos Aires and CONICET.

## References

Aitchison, J., 2003. A Concise Guide to Compositional Data Analysis. University of Glasgow, Department of Statistics, p. 134.
Andreis, R., Cúneo, R., 1985. Estratigrafía de la Formación Mojón de Hierro en puesto Garrido, extremo sudoriental de la Sierra de Tepuel, Chubut, Argentina. comunicaciones, 211. Reunión Anual Proyecto, pp. 22–24.
Andreis, R., Cúneo, R., 1989. Late Paleozoic high-constructive deltaic sequences from northwestern Patagonia, Argentina Republic. J. S. Am. Earth Sci. 2, 19–34.
Andreis, R., González, C., Cortiñas, J., 1985. Estratigrafía de los Grupo Tepuel y Río Genoa (Neopaleozoico de Chubut). Asociación Geológica Argentina, Revista 40, 284–289.
Bhatia, M.R., 1983. Plate tectonics and geochemical composition of sandstones. J. Geol. 91, 611–627.
Basu, A.R., Sharma, M., DeCelles, P.G., 1990. Nd, Sr-isotopic provenance and trace element geochemistry of Amazonian foreland basin fluvial sands, Bolivia and Peru: implications for ensialic Andean orogeny. Earth Planet Sci. Lett. 100 (1–3), 1–17.
Bradshaw, J.D., Vaughan, A.P.M., Millar, I.L., Flowerdew, M.J., Trouw, R.A.J., Fanning, C.M., Whitehouse, M.J., 2012. Permo-carboniferous conglomerates in the trinity Peninsula group at view point, antarctic Peninsula: sedimentology, geochronology and isotope evidence for provenance and tectonic setting in Gondwana. Geol. Mag. 149, 626–644.
Cerredo, M.E., López de Luchi, M.G., 1998. Mamil Choique Granitoids, southwestern North Patagonian Massif, Argentina: magmatism and metamorphism associated with a polyphasic evolution. J. S. Am. Earth Sci. 11 (5), 499–515.
Chebli, G.A., Nakayama, C., Sciutto, J., 1979. Mapa geológico de la provincia del Chubut, 1. 7° Congreso Geológico Argentino, Actas, pp. 639–655 (Neuquén).
Chen, G., Robertson, A.H., 2019. Provenance and magmatic-tectonic setting of Campanian-aged volcaniclastic sandstones of the Kannaviou Formation in western Cyprus: evidence for a South-Neotethyan continental margin volcanic arc. Sediment. Geol. 388, 114–138.
Chen, G., Robertson, A., 2020. User's guide to the interpretation of sandstones using whole-rock chemical data, exemplified by sandstones from Triassic to Miocene passive and active margin settings from the Southern Neotethys in Cyprus. Sediment. Geol. 400 https://doi.org/10.1016/j.sedgeo.2020.105616.
Ciccioli, P.L., Limarino, C.O., Taboada, A.C., Isbell, J.L., Gulbranson, E.L., 2018a. Composición modal y procedencia del Grupo Tepuel, provincia de Chubut, Argentina. VII Simposio Argentino del Paleozoico Superior, Esquel, Argentina. Suplemento Resúmenes Rev. Mus. La Plata 3, 9R–10R.
Ciccioli, P.L., Limarino, C.O., Taboada, A.C., Isbell, J.L., Gulbranson, E., 2018b. Petrología y modas detríticas de las sedimentitas neopaleozoicas de la Patagonia Extrandina, Chubut, XVI Reunión Argentina de Sedimentología, General Roca, Río Negro, vol. 43. Resúmenes.
Cortiñas, J., Arbe, H.A., 1982. Facies y paleoambientes sedimentarios del grupo Río Genoa, Pérmico Inferior de la región de Nueva Lubecka, provincia de Chubut. Rev. Asoc. Geol. Argent. 37 (3), 300–312.
Craddock, J.P., Ojakangas, R.W., Malone, D.H., Konstantinou, A., Mory, A., Bauer, W., Thomas, R.J., Affinati, S.C., Pauls, K., Zimmerman, U., Botha, G., Rochas-Campos, A., Santos, P.R.d., Tohver, E., Riccomini, C., Martin, J., Redfern, J., Horstwood, M., Gehrels, G., 2019. Detrital zircon provenance of Permo-Carboniferous glacial diamictites across Gondwana. Earth Sci. Rev. 192, 285–316.
Critelli, S., Ingersoll, R.V., 1995. Interpretation of neovolcanic versus palaeovolcanic sand grains: an example from Miocene deep-marine sandstone of the Topanga Group (Southern California). Sedimentology 42, 783–804.
Cucchi, R.J., Askenasy, T., 1982. Discontinuidad metamórfica entre las Formaciones Esquel y Valle Chico. Análisis de cristalinidad de la illita. Rev. Asoc. Geol. Argent. 37, 362–365.
Dalla Salda, L., Cingolani, C., Varela, R., 1990. The origin of Patagonia. Comunicaciones, Una revista de geología andina 41, 55–61.
Dickinson, W.R., 1970. Interpreting detrital modes of graywacke and arkose. J. Sediment. Petrol. 40, 695–707.
Dickinson, W.R., 1985. Interpreting provenance relations from detrital modes of sandstones. In: Zuffa, G.G. (Ed.), Provenance of Arenites, vol. 148. NATO Science Series C, pp. 333–361.
Dickinson, W.R., Beard, L.S., Brakenridge, G.R., Erjavec, J.L., Ferguson, R.C., Inman, K. F., Knepp, R.A., Lindberg, F.A., Ryberg, P.T., 1983. Provenance of North American Phanerozoic sandstones in relation to tectonic setting. Geol. Soc. Am. Bull. 94, 222–235.
Duhart, P., Haller, M., Hervé, F., 2002. Diamictitas como parte del protolito de las metamorfitas de la Formación Cushamen en Río Chico, Provincias de Río Negro y Chubut, Argentina. Actas del XV Congreso Geológico Argentino II:97-100. El Calafate.
Elliot, D.H., Fanning, C.M., Hulett, S.R.W., 2015. Age provinces in the Antarctic craton: evidence from detrital zircons in Permian strata from the Beardmore glacier region, Antarctica. Gondwana Res. 28 (1), 152–164.
Elliot, D.H., Fanning, C.M., Laudon, T.S., 2016. The Gondwana plate margin in the Weddell Sea sector: zircon geochronology of upper Paleozoic (mainly Permian) strata from the Ellsworth Mountains and eastern Ellsworth land, Antarctica. Gondwana Res. 29 (1), 234–247.
Escapa, I., Cúneo, R., 2003. Una nueva especie de Ginkgophyllum Saporta ex Neuburg en el Pérmico temprano de Chubut, Argentina. Rev. Mus. Argent. Ciencias Nat. Nueva Ser. 5, 181–184.
Flowerdew, M.J., Millar, I.L., Curtis, M.L., Vaughan, A.P.M., Horstwood, M.S.A., Whitehouse, M.J., Fanning, C.M., 2007. Combined U-Pb geochronology and Hf isotope geochemistry of detrital zircons from early Paleozoic sedimentary rocks, Ellsworth-Whitmore Mountains block, Antarctica. Geol. Soc. Am. Bull. 119 (3–4), 275–288.
Floyd, P., Leveridge, B., 1987. Tectonic environment of the Devonian Gramscatho basin, south Cornwall: framework mode and geochemical evidence from turbiditic sandstones. J. Geol. Soc. 144, 531–542.
Folk, R.L., Andrews, P.B., Lewis, D., 1970. Detrital sedimentary rock classification and nomenclature for use in New Zealand. N. Z. J. Geol. Geophys. 13, 937–968.
Forsythe, R., 1982. The late paleozoic to early mesozoic evolution of southern South America: a plate tectonic interpretation. J. Geol. Soc. 139, 671–682.
Garzanti, E., Resentini, A., 2016. Provenance control on chemical indices of weathering (Taiwan river sands). Sediment. Geol. 336, 81–95.
Giacosa, R., Márquez, M., Panza, J., 2002. Basamento Paleozoico inferior del Macizo del Deseado. Relatorio vol. 1. In: En Haller, M.J. (Ed.), Geología y Recursos Naturales de Santa Cruz. 15° Congreso Geológico Argentino (El Calafate), pp. 33–44. Buenos Aires, 2.
González, C., 1985. El Paleozoico superior marino de la Patagonia extraandina. Ameghiniana 21, 125–142.
González Bonorino, G., 1992. Carboniferous glaciation in Gondwana. Evidence for grounded marine ice and continental glaciation in southwestern Argentina. Palaeogeogr. Palaeoclimatol. Palaeoecol. 91, 363–375.
González Bonorino, F., González Bonorino, G., 1988. La base del Grupo Tepuel en las cercanías de Esquel, Chubut. Rev. Asoc. Geol. Argent. 43, 518–528.
González, P.D., Sato, A.M., Naipauer, M., Varela, R., Basei, M., Sato, K., Llambías, E.J., Chemale, F., Castro Dorado, A., 2018. Patagonia-Antarctica Early Paleozoic conjugate margins: Cambrian synsedimentary silicic magmatism, U-Pb dating of K-bentonites, and related volcanogenic rocks. Gondwana Res. 63, 186–225.
Griffis, N.P., Montañez, I.P., Fedorchuk, N., Isbell, J., Mundil, R., Vesely, F., Weinshultze, L., Iannuzzif, R., Gulbranson, E., Taboada, A., Pagani, A., Sanborn, M., Huyskens, M., Wimpenny, J., Linol, B., Qing-Zhu, Y., 2019. Isotopes to ice: constraining provenance of glacial deposits and ice centers in west-central Gondwana. Palaeogeogr. Palaeoclimatol. Palaeoecol. 531, 108745.
Harrington, H.J., 1962. Paleogeographic development of South America. Tulsa Am. Assoc. Petrol. Geol. Bull. 46 (10), 1773–1814.
Herron, M.M., 1988. Geochemical classification of terrigenous sands and shales from core or log data. J. Sediment. Res. 58, 820–929.
Hervé, F., Fanning, C.M., Pankhurst, R.J., 2003. Detrital zircon age patterns and provenance of the metamorphic complexes of southern Chile. J. S. Am. Earth Sci. 16, 107–123.
Hervé, F., Haller, M.J., Duhart, P., Fanning, C.M., 2005. SHRIMP U-Pb ages of detrital zircons from Cushamen and Esquel formations, North Patagonian Massif, Argentina: geological implications. Actas XVI. Congreso Geológico Argentino (La Plata), pp. 309–314.
Hervé, F., Calderón, M., Fanning, C.M., Pankhurst, R.J., Godoy, E., 2013. Provenance variations in the Late Paleozoic accretionary complex of Central Chile as indicated by detrital zircons. Gondwana Res. 23, 1122–1135.
Hervé, F., Calderon, M., Fanning, C.M., Pankhurst, R.J., Fuentes, F., Rapela, C.W., Correa, J., Quezada, P., Marambio, C., 2016. Devonian magmatism in the accretionary complex of southern Chile. J. Geol. Soc. 173 (4), 587–602.
Hervé, F., Calderon, M., Fanning, C.M., Pankhurst, R.J., Fuentes, F., Rapela, C.W., Quezada, P., 2018. The country rocks of devonian magmatism in the north patagonian massif and chaitenia. Andean Geol. 45 (3), 301–317.
Ingersoll, R., Cavazza, W., 1991. Reconstruction of Oligo-Miocene volcaniclastic dispersal patterns in north-central New Mexico using sandstone petrofacies. SEPM (Soc. Sediment. Geol.) Spec. Publ. 45, 227–236.
Isbell, J.L., Lenaker, P.A., Askin, R.A., Miller, M.F., Babcock, L.E., 2003. Reevaluation of the timing and extent of late paleozoic glaciation in Gondwana: role of the transantarctic Mountains. Geology 31 (11), 977–980.
Isbell, J.L., Henry, L.C., Gulbranson, E.L., Limarino, C.O., Fraiser, M.L., Koch, Z.J., Ciccioli, P.L., Dineen, A.A., 2012. Glacial paradoxes during the late Paleozoic ice age: evaluating the equilibrium line altitude as a control on glaciation. Gondwana Res. 22 (1), 1–19.
Jahn, B.M., Condie, K.C., 1995. Evolution of the Kaapvaal Craton as viewed from geochemical and Sm-Nd isotopic analyses of intracratonic pelites. Geochem. Cosmochim. Acta 59, 2239–2258.
Kostadinoff, J., Gregori, D.A., Raniolo, A., 2005. Configuración geofísica-geológica del sector norte de la provincia de Río Negro. Asociación Geológica Argentina, Revista 60 (2), 368–376.

Limarino, C.O., Giordano, S.R., 2016. Unraveling multiple provenance areas using sandstone petrofacies and geochemistry: an example in the southern flank of the Golfo San Jorge Basin (Patagonia, Argentina). J. S. Am. Earth Sci. 66, 208–231.
Limarino, C.O., Massabie, A., Rossello, E., López Gamundí, O.L., Page, R., Jalfin, G., 1999. El Paleozoica de Ventania, Patagonia e Islas Malvinas. In: Caminos, R. (Ed.), Geología Argentina, pp. 319–348 (Buenos Aires).
Limarino, C.O., Ciccioli, P.L., Taboada, A.C., Vizán, H., 2020a. Secuencias sedimentarias del Paleozoico. Relatorio de Geología y Recursos Naturales de la Provincia del Chubut, vol. XXI. Congreso Geológico Argentino, Puerto Madryn (in press).
Limarino, C.O., Giordano, S.R., Rodriguez Albertani, R., Ciccioli, P.L., Bodan, F., 2020b. Patterns and origins of the porosity in the productive reservoirs of the upper part of the chubut group, southern flank of the golfo de San jorge basin, Patagonia Argentina". J. S. Am. Earth Sci. 98, 102480. https://doi.org/10.1016/j.jsames.2019 (in press).
López Gamundí, O.R., 1980. La Formación Esquel, litología y estructura. Provincia del Chubut. Rev. Asoc. Geol. Argent. 35, 187–194.
López Gamundí, O.R., 1989. Postglacial transgressions in Late Paleozoic basins of western Argentina: a record of glacioeustatic sea level rise. Palaeogeogr. Palaeoclimatol. Palaeoecol. 71 (3–4), 257–270.
López Gamundí, O.R., Limarino, C.O., 1984. Facies de abanico submarino en el Grupo Tepuel (Paleozoico superior), provincia de Chubut. Rev. Asoc. Geol. Argent. 39, 251–261.
López-Gamundí, O.R., Limarino, C.O., Cesari, S.N., 1992. Late Paleozoic paleoclimatology of central west Argentina. Palaeogeogr. Palaeoclimatol. Palaeoecol. 91 (3–4), 305–329.
Marcos, P., Gregori, D.A., Benedini, L., Barros, M., Strazzere, L., Pivetta, C.P., 2018. Pennsylvanian glacimarine sedimentation in the Cushamen Formation, western North Patagonian massif. Geoscience Frontiers 9 (2), 485–504.
Martínez, J.C., Dristas, J.A., Massonne, H.J., 2012. Paleozoic accretion of the microcontinent Chilenia, North Patagonian Andes: high-pressure metamorphism and subsequent thermal relaxation. Int. Geol. Rev. 54 (4), 472–490.
McLennan, S.M., 1989. Rare earth elements in sedimentary rocks: influence of provenance and sedimentary processes. Rev. Mineral. 21, 169–200.
McLennan, S.M., Hemming, S., McDaniel, D.K., Hanson, G.N., 1993. Geochemical Approaches to Sedimentation, Provenance, and Tectonics. Special Papers-Geological Society of America, p. 21, 21.
McNall, N.B., 2019. Sedimentological and geochemical analysis of deep-water deposits in the Mojón de Hierro Formation at Arroyo Garrido, Tepuel-Genoa Basin, Patagonia, Argentina. M.S. Thesis. Department of Geosciences. University of Wisconsin-Milwaukee, Milwaukee, Misconsin, p. 124.
Moreira, P., González, P.D., Fernández, R., Echeveste, H., Schalamuk, I., Etcheverry, R., 2005. El basamento metamórfico de muy bajo a bajo grado de las estancias La Modesta y La Josefina, macizo del Deseado, provincia de Santa Cruz, 0 Rev. Asoc. Geol. Argent. 60 (1), 49–63, 0.
Nesbitt, H.W., Young, G., 1984. Prediction of some weathering trends of plutonic and volcanic rocks based on thermodynamic and kinetic considerations. Geochem. Cosmochim. Acta 48, 1523–1534.
Net, L.I., Limarino, C.O., 2006. Applying sandstone petrofacies to unravel the Upper Carboniferous evolution of the Paganzo Basin, northwest Argentina. J. S. Am. Earth Sci. 22 (3–4), 239–254.
Page, R., Limarino, C., López Gamundí, O., Page, S., 1984. Estratigrafía del Grupo Tepuel en su perfil tipo y en la región de El Molle, provincia del Chubut, vol. 1. 9° Congreso Geológico Argentino, Actas, pp. 619–632 (San Carlos de Bariloche).
Pankhurst, R.J., Rapela, C.W., Loske, W.P., Marquez, M., Fanning, C.M., 2003. Chronological study of the pre-Permian basement rocks of southern Patagonia. J. S. Am. Earth Sci. 16, 27–44.
Pankhurst, R.J., Rapela, C.W., Fanning, C.M., Márquez, M., 2006. Gondwanide continental collision and the origin of Patagonia. Earth Sci. Rev. 76, 235–257.
Pauls, K.N., Thesis, M.S., 2014. Sedimentology and Paleoecology of Fossil-Bearing, High-Latitude Marine and Glacially Influenced Deposits in the Tepuel Basin, Patagonia, Argentina. Department of Geosciences. University of Wisconsin-Milwaukee, Milwaukee, Wisconsin, p. 157.
Pettijohn, F.J., Potter, P.E., Siever, R., 1972. Sand and Sandstone. Springer-Verlag, New York, p. 553.
Ramos, V.A., 1984. Patagonia: ¿Un continente paleozoico a la deriva? 9th Congreso Geológico Argentino, Bariloche, Actas 2, 311–325.
Ramos, V.A., 1996. Evolución tectónica de la Plataforma continental. In: Ramos, V.A., Turic, M.A. (Eds.), Geología y Recursos Naturales de la Plataforma Continental Argentina. Asociación Geológica Argentina e Instituto Argentino del Petróleo, Buenos Aires, pp. 359–368.
Ramos, V.A., 2008. Patagonia: a Paleozoic continent a drift? J. S. Am. Earth Sci. 26, 235–251.
Ramos, V.A., Naipauer, M., 2014. Patagonia: where does it come from? J. Iber. Geol. 40, 367–379.
Ramos, V.A., Jordan, T.E., Allmendinger, R.W., Mpodozis, C., Kay, S.M., Cortés, J., Palma, M., 1986. Paleozoic terranes of the central Argentine Chilean Andes. Tectonics 5, 855–880.
Rapalini, A.E., de Luchi, M.L., Dopico, C.M., Klinger, F.L., Giménez, M.E., Martínez, P., 2010. Did Patagonia collide with Gondwana in the late paleozoic? Some insights from a multidisciplinary study of magmatic units of the north patagonian massif. Geol. Acta 8 (4), 349–371.
Renda, E.M., Alvarez, D., Prezzi, C., Oriolo, S., Vizán, H., 2019. Inherited basement structures and their influence in foreland evolution: a case study in Central Patagonia, Argentina. Tectonophysics 772, 228–232.
Roser, B.P., Korsch, R.J., 1986. Determination of tectonic setting of sandstone-mudstone suites using SiO2 content and K2O/Na2O ratio. J. Geol. 94 (5), 635–650.
Roser, B.P., Korsch, R.J., 1988. Provenance signatures of sandstone-mudstone suites determined using discriminant function analysis of major-element data. Chem. Geol. 67, 119–139.
Roser, B.P., Coombs, D.S., Korsch, R.J., Campbell, J.D., 2002. Whole-rock geochemical variations and evolution of the arc-derived Murihiku Terrane, New Zealand. Geol. Mag. 139, 665–685.
Sidgel, A., Sakai, T., 2013. Petrography of Miocene Siwalik Group sandstones, Karnali River section, Nepal Himalaya: implications for source lithology and tectonic setting. J. Nepal Geol. Soc. 46, 95–110.
Simanauskas, T., Sabattini, N., 1997. Bioestratigrafía del Paleozoico Superior marino de la Cuenca Tepuel-Genoa, provincia del Chubut, Argentina. Ameghiniana 34, 49–60.
Spalletti, L.A., Schwarz, E., Veiga, G.D., 2014. Geoquímica inorgánica como indicador de procedencia y ambiente sedimentario en sucesiones de lutitas negras: los depósitos transgresivos titonianos (Formación Vaca Muerta) de la Cuenca Neuquina, Argentina. Andean Geol. 41 (2), 401–435.
Suero, T., 1953. Las sucesiones sedimentarias suprapaleozoicas de la zona extraandina del Chubut (Patagonia Austral, República Argentina). Rev. Asoc. Geol. Argent. 8 (1), 37–53.
Survis, S.R., 2015. Sedimentology and stratigraphy of high-latitude, glacigenic deposits from the late Paleozoic Ice Age. In the Tepuel-Genoa Basin, Patagonia, Argentina. M. S. Thesis, Department of Geosciences. University of Wisconsin-Milwaukee, Wisconsin, p. 90.
Taboada, A.C., Taboada, C.A., Pardo, C.A., Césari, S., 2018. Formación Valle Chico, Esquel, Chubut: actualización del registro paleontológico, discusión estratigráfica e implicancias paleoclimáticas. Suplemento Resúmenes 20R-21R Simposio Argentino del Paleozoico Superior, No. 7. Revista del Museo de La Plata, Esquel.
Taboada, A.C., Pagani, M.A., Pinilla, M.K., Tortello, M.F., Taboada, C.A., 2019. Carboniferous deposits of northern Sierra de Tecka, central-western Patagonia, Argentina: paleontology, biostratigraphy and correlations. Andean Geol.: Formerly Revista geológica de Chile 46 (3), 629–669.
Taylor, S.R., McLennan, S.M., 1985. The Continental Crust: its Composition and Evolution. Blackwell Scientific Publications, United States, p. 312.
Verma, S.P., Armstrong-Altrin, J.S., 2016. Geochemical discrimination of siliciclastic sediments from active and passive margin settings. Sediment. Geol. 332, 1–12.
Viera, R., Pezzuchi, H., 1976. Presencia de sedimentitas pérmicas en contacto con rocas del ··Complejo metamórficoö de la Patagonia extrandina, Ea dos Hermanos, provincia de Santa Cruz. Revista Asociación Geológica Argentina 31 (4), 281–283.
Weltje, G.J., 2002. Quantitative analysis of detrital modes: statistically rigorous confidence regions in ternary diagrams and their use in sedimentary petrology. Earth Sci. Rev. 57, 211–253.
Winter, H.R., 1984. Tectonostratigraphy as applied to analysis of South African Phanerozoic basin. Trans. Geol. Soc. S. Afr. 87, 169–179.
Yakymchuk, C., Brown, C.R., Brown, M., Siddoway, C.S., Fanning, C.M., Korhonen, F.J., 2015. Paleozoic evolution of western Marie Byrd land, Antarctica. Geol. Soc. Am. Bull. 127, 1464–1484.
Zhang, Y., Pe-Piper, G., Piper, D.J., 2014. Sediment geochemistry as a provenance indicator: unravelling the cryptic signatures of polycyclic sources, climate change, tectonism and volcanism. Sedimentology 61 (2), 383–410.
Zuffa, G.G., 1985. Optical analyses of arenites: influence of methodology on compositional results. In: Zuffa, G.G. (Ed.), Provenance of Arenites. NATO-ASI Ser., Ser. C. , Reidel Publ., Dordrecht, pp. 165–189.